UNIVERSITY OF CALIFORNIA

Los Angeles

Design and applications of Kerr frequency combs

A thesis submitted in partial satisfaction

of the requirements for the degree Master of Science

in Electrical and Computer Engineering

by

Tristan Roger Melton

2023

ABSTRACT OF THE THESIS

Design and applications of Kerr frequency combs

by

Tristan Roger Melton

Master of Science in Electrical and Computer Engineering

University of California, Los Angeles, 2023

Professor Chee Wei Wong, Chair

Optical frequency combs have become a major source of innovation in a wide array of fields such as metrology, ultrafast optics, and light-matter interactions. Specifically, Kerr frequency combs have risen to the forefront of comb sources in applications requiring small size, light weight, and relatively low power consumption (SWaP). The design and generation of Kerr frequency combs at 1-micron and their application in frequency-domain optical coherence tomography (FD-OCT) and microwave generation are explored. Microresonators are designed in a silicon nitride platform to generate octave-spanning comb states. Then, various comb states are generated at this wavelength to explore comb dynamics, including stabilization. Platicon combs are also examined at 1600-nm. Finally, 1-μm Kerr frequency comb FD-OCT with comparable image quality to that of a traditional superluminescent diode FD-OCT is demonstrated with an effective axial resolution that approaches the theoretical limit.

The thesis of Tristan Roger Melton is approved.

Chandrashekhar Janar Joshi

Mona Jarrahi

Chee Wei Wong, Committee Chair

University of California, Los Angeles

2023

CONTENTS

LIST OF FIGURES

LIST OF FIGURES

ACKNOWLEDGEMENTS

Sections 2 through 5 are a version of [T. Melton, J. McMillan, W. Wang, Y. Lai, M. Gerber, M. Rodriguez, K. Nouri-Mahdavi, J.P. Hubschman, and C. W. Wong, “High-Resolution Millimeter-Depth Optical Coherence Tomography with 1-um 100-GHz Chip-Scale Laser Frequency Microcombs,” in *CLEO: 2022* (Optical Society of America, Washington DC, 2022), 3691246], which is submitted for publication.

Section 6 is a version of [W. Wang, J. Lim, T. Melton, A. Aldhafeeri, A. K. Vinod, J. Yang, M. Yu, D.-L. Kwong, and C. W. Wong, “Spontaneous microwave platicon frequency mirocomb in dispersion-managed microresonators”, (2024)], which is under review (2024).

1 INTRODUCTION

1.1 INTRODUCTION TO FREQUENCY COMBS

An optical frequency comb is a light source comprised of equally spaced narrow Lorentzian lines spanning some bandwidth. Comb lines are inherently very stable at their center frequency and therefore can be used for a wide variety of applications within the field of spectroscopy and metrology [1]. Frequency combs can be generated in a multitude of ways with one common method utilizing mode-locked lasers, and nonlinearities via four wave mixing and other Kerr effects. Recent developments in nonlinear optics have led to the introduction of high-Q, anomalous-dispersion microresonators capable of generating these combs called Kerr frequency combs [2]. The comb structure can be explained by realizing the propagation of a pulse in a cavity has a repetition rate f_{rep}dependent on the optical length and the refractive index of the cavity – in frequency space, this pulse would have a comb structure, with each comb line spaced by f_{rep}. Every round trip, a phase slip between the carrier and envelope occurs and by measuring the speed of the change of the slip, the carrier envelope offset frequency, f_{ceo} is defined [1,2]. With these two terms, the absolute frequency of each comb line is defined as

$$f_m = f_{ceo} + m * f_{rep}, \tag{1}$$

where m is some positive integer, denoting the comb modes.

Generally, comb formation begins with four wave mixing, with some spacing relative to the pump dependent on intracavity power, cavity dispersion and the pump detuning. Further detuning the pump laser into the resonance results in cascaded four wave mixing, forming what is known as the Turing pattern, or primary comb lines. At these primary comb lines the four wave mixing process most efficient, and further detuning causes secondary groups of lines to

form around each of these primary lines via a combination of degenerate and non-degenerate four wave mixing, creating what are known as sub-combs surrounding each primary comb line with spacing equal to that of the free spectral range of the cavity. As the power coupled into the cavity continues to increase, the sub-combs merge into a full, gap-free smooth envelope spectrum of lines. When the proper balance of parametric gain versus cavity losses and nonlinear phase shift versus group velocity dispersion (GVD) of the microresonator are achieved, mode-locked pulses called dissipative Kerr solitons can be reliably and stably generated. These pulses are self-reinforcing wave packets that do not broaden or change shape as they propagate within the ring waveguide, enabling pulsed laser sources on-chip and furthering development of chip-scale photonic technologies.

Due to strong thermal effects within the microresonator, simple manual detuning into the soliton state is challenging and an unreliable method of formation – because solitonic states have lower intracavity power than the chaotic states at earlier detunings, the sudden drop in power when tuning into a soliton state results in a strong thermal shift of the resonances which can push the pump laser out of the soliton existence range. Fast detuning can prove effective given the pump laser can be stopped precisely at the point of soliton formation without excessive cavity heating but can be technically challenging [3]. Alternatively, an auxiliary laser can be coupled to a distant resonance and sent counter-propagating to the main pump as a method of thermal stabilization [4]. As the main pump drops into the soliton state, resonances shift to lower wavelength due to lower intracavity power from the main pump. At the same time, this results in the effective detuning of the auxiliary pump to increase, increasing the total intracavity power due to the auxiliary laser. When properly balanced, only a small thermal-induced shift of the resonances occurs and the soliton state is stably accessed.

1.2 APPLICATION

Optical frequency combs have unique potential in several applications, which is briefly discussed here and expounded upon in the rest of this thesis. When soliton states are generated, the resultant pulse train can be used as a high-quality clock for synchronization and timing [5]. In this way, they can also act as an optical-to-microwave clockwork for microwave generation [6, 7, 8]. Their unique spectral characteristics can also be utilized as a source for frequency comb spectroscopy [9, 10]. Because Kerr frequency microcombs have small size, light weight, and relatively low power consumption (SWaP) and can reach bandwidths exceeding an octave with proper engineering, they are an attractive broadband light source for discrete Spectral Domain Optical Coherence Tomography (SD-OCT) [11]. In addition, microcombs can be generated over the range of wavelengths supported by the underlying material nonlinear properties and engineered dispersion profile, allowing a larger range of comb generation frequencies. This lends to their integration in SD-OCT systems as a cheaper, longer lasting, and potentially higher resolution alternative to traditional broadband sources [11]. This work examines frequency combs as ultra-low phase noise radio frequency (RF) source and their application within FD-OCT as an alternative to superluminescent diodes (SLD).

2 DESIGN OF MICRORESONATORS FOR KERR COMB GENERATION

2.1 BACKGROUND

Frequency combs require modal confinement in a high quality factor (Q) resonator with a strong nonlinear coefficient for generation. Many materials such as silica [12, 13, 14], silicon nitride [15, 16, 17-29], aluminum nitride [30], diamond [31], AlGaAs [32], and crystalline fluorides [33, 34] have been demonstrated to possess strong nonlinear parameters to generate

such comb structures. In this section, the purpose of the microresonator is to generate a dispersive Kerr soliton with octave-spanning bandwidth for fully self-referenced comb stabilization [35, 36]. To perform full detection and stabilization of f_{rep} and f_{ceo}, a f-$2f$ detection scheme is chosen such that comb light at frequency f is frequency doubled to $2f$ and then beat against corresponding comb lines at $f_2 = 2f$, allowing for f_{ceo} to be detected [35-37]:

$$f = n f_{rep} + f_{ceo} \tag{2}$$

$$f_2 = 2n f_{rep} + f_{ceo} \tag{3}$$

$$2f - f_2 = f_{ceo} \tag{4}$$

The pump laser is inherently locked to the soliton – by locking f_{ceo}, a two-point lock is effectively implemented. Additionally, the large mode spacing between the pump and f_{ceo} further reduces the repetition rate noise by a factor of N, where N is the number of modes between the two locked modes [35-37]. If f_{rep} is outside of common photodetector bandwidth and the goal is to directly lock it, it can be measured and stabilized independently by generating sidebands on the comb teeth via electro-optic modulation, after which the beat between the two EO-comb teeth directly between the main comb lines can be filtered, detected, and used as a locking signal [35, 36]. In this work, silicon nitride (SiN) is chosen for its compatibility with CMOS processes, high realized Q, and high third-order nonlinear coefficient [17-29]. Although increasing the free spectral range of the resonator will increase the bandwidth, smaller rings will increase bending loss and degrade the device Q making it unreasonable to obtain high power comb lines at the octave-spanning points, critical for self-referenced comb stabilization [36]. Instead, dispersive waves which appear where the GVD profile with respect to wavelength crosses zero can be engineered to generate at the octave-spanning points, improving the local optical power [38].

These spectral features are mode-locked to the main soliton and therefore can be used for the octave-spanning locking technique mentioned prior. Therefore, key to the generation the desired soliton state is proper microresonator design to achieve an anomalous GVD with dispersive waves at the proper positions. By adjusting the cross-sectional dimensions of the microresonator waveguide, the GVD can be tailored to the desired sign and magnitude at a given wavelength range. Practically, for most foundries supporting SiN, the height is fixed by the process flow and only the waveguide width is available for adjustment. The radius of the microring determines the free spectral range (FSR) of the resulting comb and has control over f_{ceo}, with only minor influence on the dispersion properties of the device [37]. The bus waveguide width in combination with the ring-to-bus gap determines the coupling conditions to the device. Based on information provided by the foundry, an estimated quality factor is established for the rings and the coupling from the bus to microring is optimized to match this loss, achieving critical coupling to the device. Once proper device geometry is obtained, small variations in ring width and coupling gap are implemented in the layout design to account for fabrication error.

2.2 DISPERSION ENGINEERING OF RING RESONATORS

To fully lock the soliton, comb power at an octave is required [35, 36]. Operation wavelength is chosen as 1-μm to place octave-spanning lines at 775-nm and 1550-nm, wavelengths convenient for second harmonic generation (SHG) and for photodetection, via dispersive waves. A device FSR of 1-THz is chosen to enable this broadband, octave-spanning microcomb state, which corresponds to a ring radius of approximately 22.5-μm. An axisymmetric finite-element method (FEM) simulation is performed utilizing COMSOL Multiphysics to simulate the modal profiles and extract the effective refractive index as a function of frequency varying ring width and height. The simulation results are then processed in

MATLAB to plot GVD and the integrated dispersion, D_{int} versus wavelength curves for different ring waveguide dimensions. Dispersive wave positions can be extracted from the GVD plots and f-2f crossing points are additionally plotted. This process is iteratively performed until the desired GVD profile and dispersive wave positions are found. Once an appropriate ring waveguide design is located, the gap between the bus waveguide and ring is swept and the coupling rate for the desired pump wavelength is found via a FDTD simulation performed in Ansys Lumerical. Devices are then implemented in GDSII format utilizing Python in accordance with foundry limitations and guidelines and sent to be fabricated at LiGenTec in Switzerland.

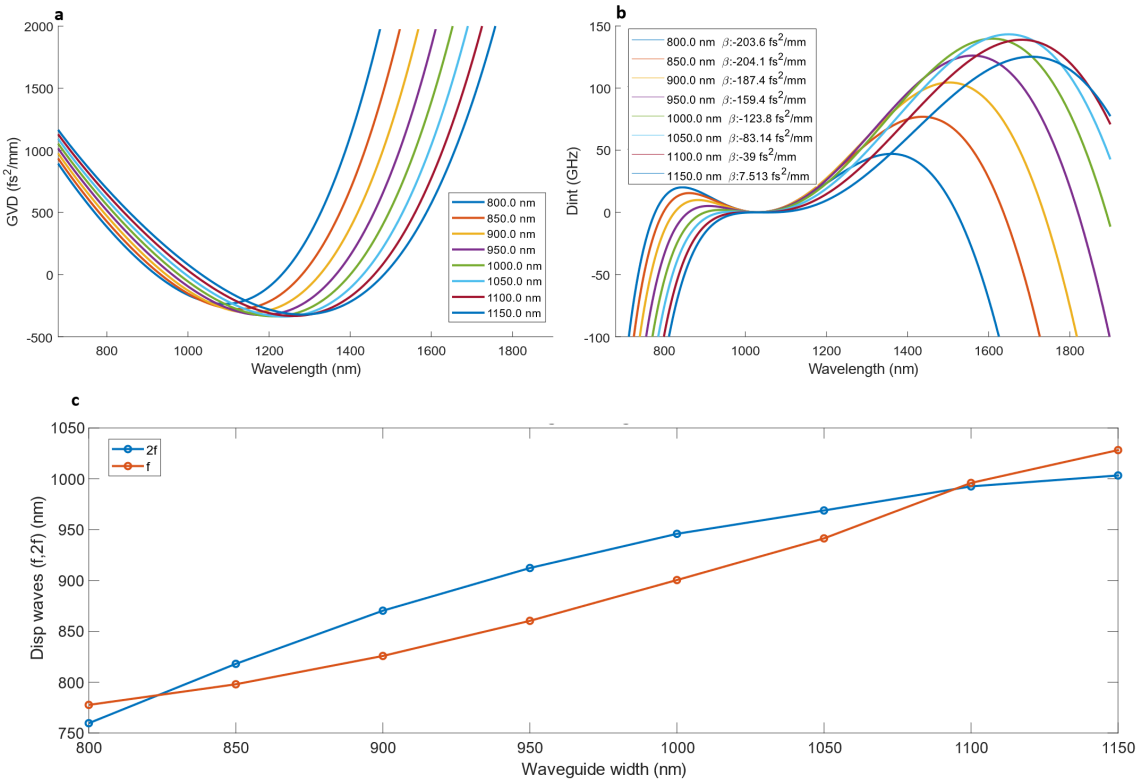

Figure 1| Simulated frequency comb dispersion characteristics. (a) Simulated GVD of 1-THz microresonators with varying ring widths. (b) Simulated Dint of 1-THz microresonators with varying ring width, with corresponding β_2. (c) Simulated dispersive wave positions for varying

ring waveguide width. Dispersive waves align at an octave at a ring width of approximately 825-nm and again at approximately 1080-nm.

3 GENERATION AND ANALYSIS OF KERR SOLITONS

3.1 COMB RESULTS OF FABRICATED DEVICES

Once chiplets are received the average loaded Q of the devices are measured to be approximately 600,000. The devices are pumped at 1064-nm with an auxiliary laser at 1030-nm for soliton stabilization [21, 23, 4]. The auxiliary laser is tuned into resonance such that it generates the early stages of a full chaotic comb. Then, the main pump is slowly tuned from the blue side to red side of a separate resonance. Initially, the main pump enters the resonance such that it generates the Turing pattern and sub-combs, shown in Figure 2a as Δ_0. Detuning increases to Δ_1, where sub-combs begin to merge and the full comb begins to form. By Δ_2, a full frequency comb has formed but is not a soliton, evidenced by the noisy electrical spectrum caused by beating between the sub-combs. If the auxiliary pump is sufficiently tuned into its resonance such that an appropriate amount of power is in the cavity to perform the thermal balancing, single and multiple soliton states can be accessed with further detuning (Δ_3, Δ_4, Δ_5) which exist on the red detuned side of the main pump resonance.

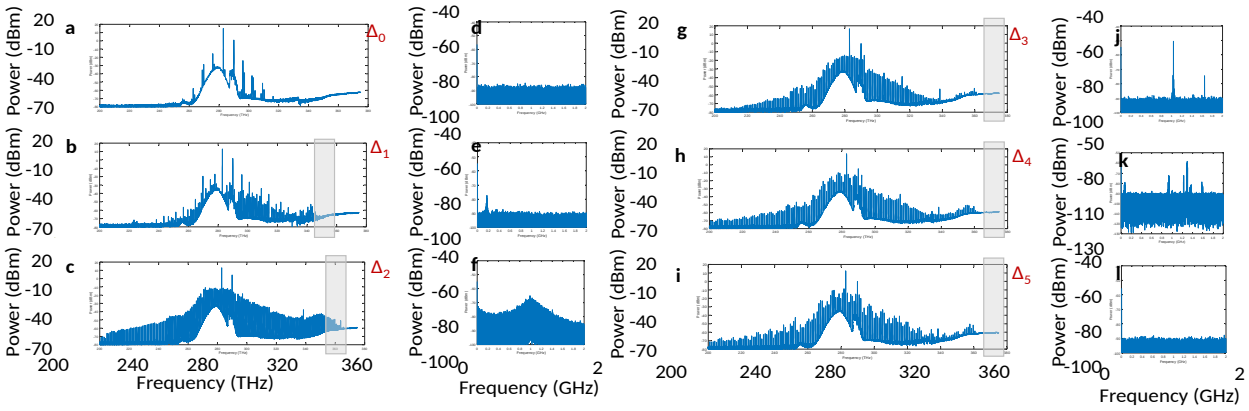

Figure 2| Generated frequency combs and electrical spectra. (a-c, g-i) Frequency comb spectra with increasing detuning. Order of state generation is indicated by the subscript of Δ. The comb state evolves from Turing pattern (a), multiple subcombs (b), full chaotic comb (c), single soliton with breather frequency (g), dual soliton with breather frequency (h), and multi-soliton state (i). Dispersive waves present in the comb states are bounded by a gray box. (d-f, j-l) Electric spectra of corresponding frequency combs. Panels (e) and (f) show the broad, low-frequency tone characteristic of a chaotic comb, (j) and (k) show breather tones and beating between the two pumps in a solitonic state, and (l) confirms a quiet comb state.

When properly thermally stabilized, the soliton states last for several hours, only dropping due to the end of an experiment or strong environmental disturbance. Dispersive waves are generated in devices of differing ring widths, with the short frequency dispersive wave at smaller ring width and long frequency dispersive wave at high ring width [22]. Due to suboptimal bus to ring coupling, a device with both dispersive waves is not yet located but search is ongoing.

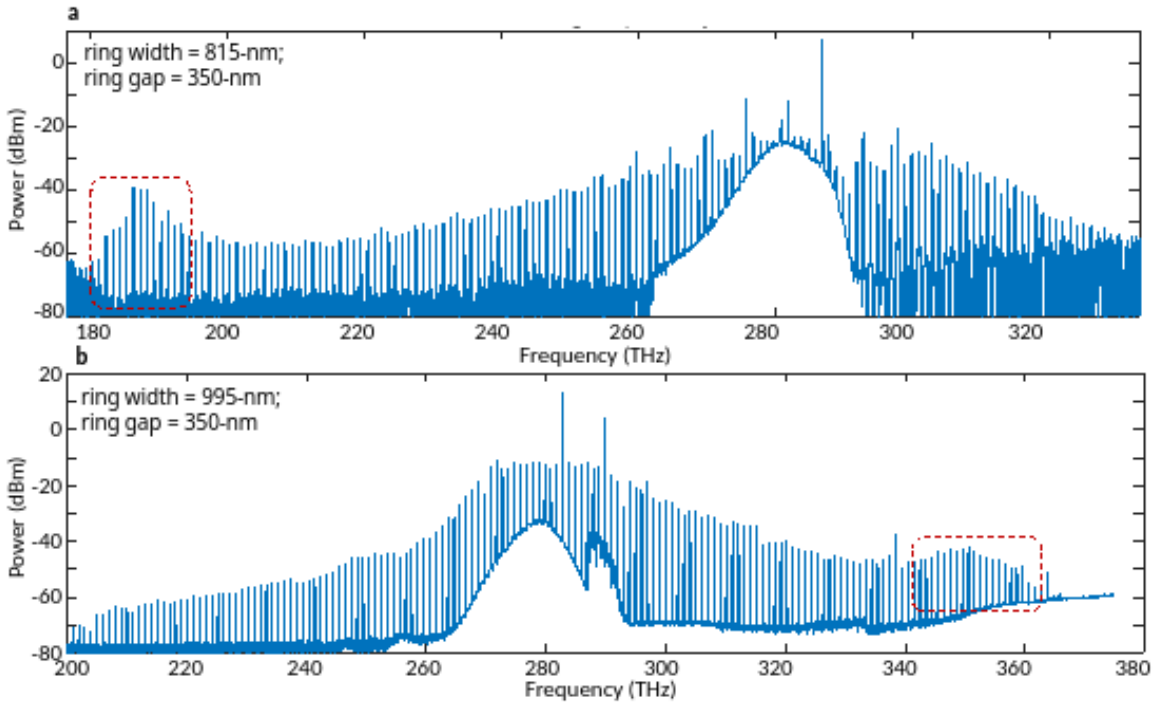

Figure 3| Broad frequency comb states with dispersive waves. Dispersive waves are shown in red dashed boxes. (a) Chaotic frequency comb with low-frequency dispersive wave at approximately 190-THz. (b) Chaotic frequency comb with high-frequency dispersive wave at approximately 350-THz.

3.2 STABILIZATION OF REPETITION RATE

Once a suitable soliton state is generated, the repetition rate is stabilized through optical and microwave frequency division to probe the phase noise limitations of our microring [35, 39]. Comb lines are passed through a series of phase modulators to generate an electro-optic comb with a modulation frequency at 12.645GHz. The relative phase between the modulators is adjusted to optimize the spectral power to be in the exact middle of the two soliton comb lines.

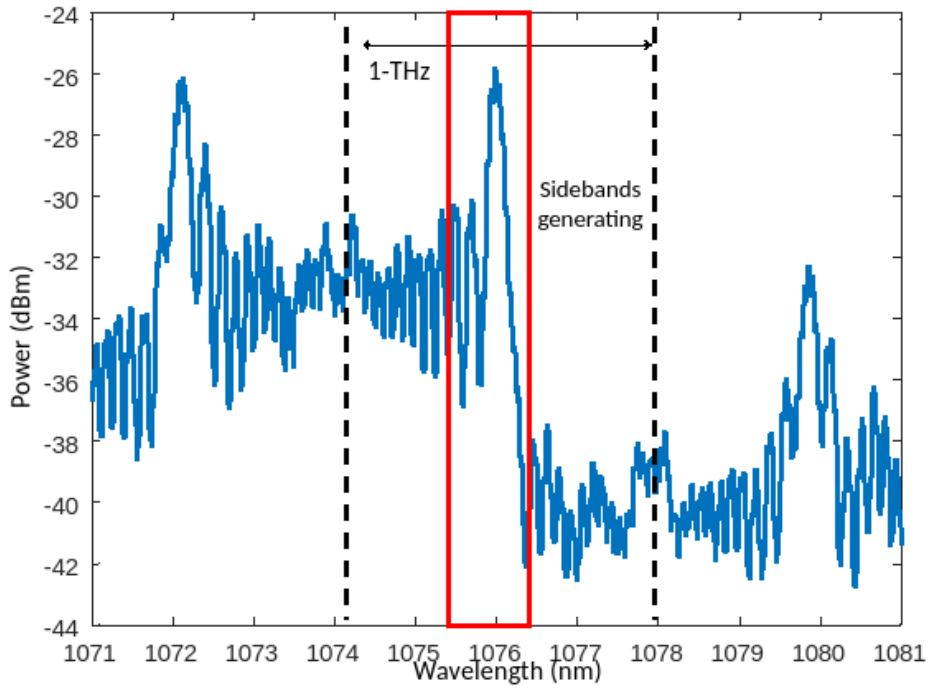

Figure 4| Modulation of soliton comb for f_{rep} measurement. A modulation frequency of 12.656-GHz is applied to the soliton with four sequential phase modulators driven by high-power electrical amplifiers. The sidebands span 1-THz and are optimized such that a peak appears at the midpoint between each pair of neighboring comb lines.

A series of optical filters isolate the beat note to improve the photodetected signal signal-to-noise ratio (SNR). After a series of RF components, the signal is digitally divided to improve signal noise and locking conditions. A Vescent lockbox is used to stabilize and lock the signal. The divisor is reduced from 260 to 25, then from 25 to 8 as the optical SNR is optimized to improve the sensitivity of the lock. A phase noise of -130dBc/Hz is achieved, limited by the SNR of the optical signal preventing further improvement of the lock sensitivity by removal of the RF division stage. Further optimization of the optical SNR is ongoing.

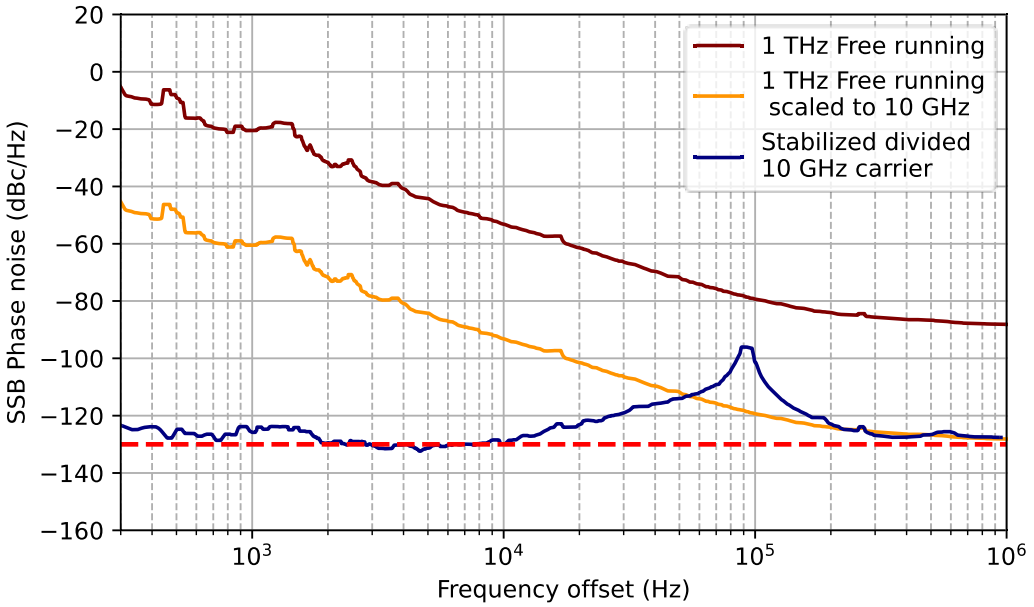

Figure 5| Phase noise measurement of repetition rate. At a 10-kHz offset with the frequency scaled to 10-GHz, a phase noise of -130-dBc/Hz is achieved (marked by a dashed red line). The peak at 90-kHz corresponds to the servo bump introduced by the lockbox.

3.3 CALCULATION OF f_{rep} AND f_{ceo}

With a soft lower bound on the phase noise, now control of f_{ceo} is shown for optimization towards a detectable frequency. Both f_{rep} and f_{ceo} can be calculated from the frequency comb spectrum, utilizing Equation 2. f_{rep} can be calculated by measuring the comb line spacing between each mode of the frequency comb, if unable to be measured directly. The measurement of the center offset frequency f_{ceo}requires an octave-spanning comb with significant power at f-$2f$. However, to calculate f_{ceo}, a measurement or calculation of f_{rep} is the only required additional information to the comb spectrum. Changing the ring radius will slightly perturb the FSR which causes a change in f_{ceo} due to the modified comb line spacing without significantly changing the GVD of the resonator. To perform these calculations, chaotic frequency combs are

generated in a set of devices with ring radius from 22.10-μm to 22.90-μm. Each comb spectrum is saved and f_{rep} is calculated for each state. A slope of the best fit line is calculated to be -4.6-GHz per 100-nm.

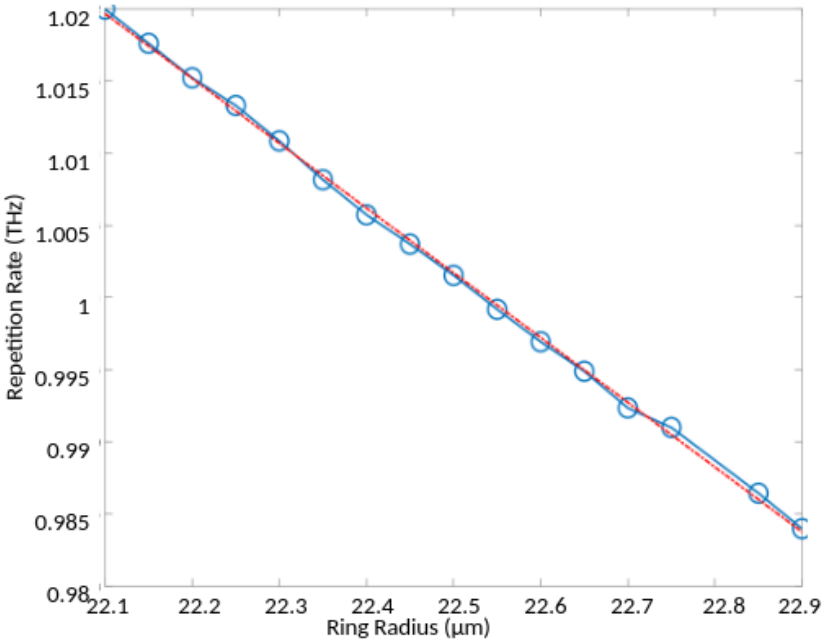

Figure 6| Calculated repetition rate of frequency comb. As ring radius increases, comb FSR decreases at a rate of approximately -4.6-GHz per 100-nm. The fit is shown as a dashed red line.

Then, for each comb line in each spectrum, the comb line number n is calculated and f_{ceo} is calculated from Equation 2. The slope of the best-fit line is calculated to be 159-GHz per 100nm. In this way, broad control of f_{ceo} with ring geometry is demonstrated without strong effects on the comb repetition rate.

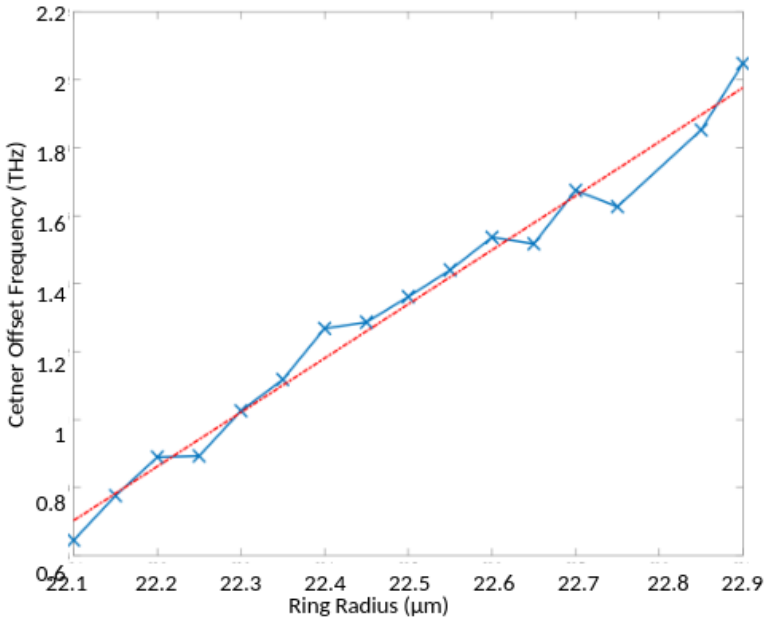

Figure 7| Calculated center offset frequency of frequency comb. As ring radius increases, the center offset frequency also increases at a rate of 159-GHz per 100-nm. The best-fit line is shown as a red dashed line. Although f_{ceo} cannot exceed half of the FSR, here it is shown unwrapped for clarity of presentation.

4 MEASUREMENT DETAILS

4.1 DETAILS OF THE SOLITON GENERATION SETUP

A Toptica CTL1050 is utilized as the main pump laser and Sacher Lasertechnik Lion TEC-500-1060-030-M is utilized as an auxiliary stabilization laser. The main pump is amplified by an Amonics Ytterbium doped fiber amplifier (YDFA) to 27.5dBm and the auxiliary is amplified by a BKTEL YDFA to 30dBm. Both lasers pass through separate circulators to separate the pump from the outgoing comb light from the other respective pump. Light is coupled into the chip with lensed fibers, with the main and auxiliary lasers counter-propagating. The third port of each circulator is used to monitor comb power and state via a power meter and optical spectrum

analyzer (OSA). The main laser is placed far in the red detuning regime from a resonance while the auxiliary laser is tuned into resonance such that it generates a partial chaotic comb. Once this state is achieved, the main pump is backwards detuned into the resonance at which point some number of solitons will appear. A backwards detuning technique [40] is employed to reduce the state to a single soliton.

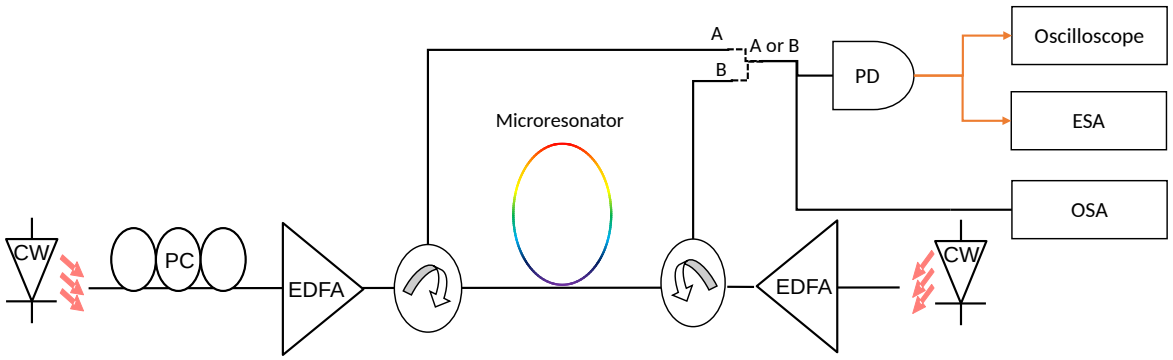

Figure 8| Frequency comb generation setup. The microring is dual-pumped by two amplified lasers for stable soliton generation. Circulators isolate the forward and backward propagating light which then is passed to a photodetector for electrical analysis and optical spectrum analyzer to observe the comb state.

4.2 DETAILS OF THE f_{rep} STABILIZATION SETUP

The soliton state is passed through fiber Bragg gratings to remove the pump and auxiliary before being amplified to improve comb SNR. Two comb teeth are filtered with 1-nm tunable optical filters, which then pass through three phase modulators driven by high power RF amplifiers to generate 41 pairs of sidebands. The central peak is broadly filtered with a 3-nm tunable filter before a second set of 1-nm tunable filters further eliminates unwanted optical signal after which the optical signal is amplified and photodetected. The resulting RF signal is tuned to 907-MHz by fine-tuning the EO modulation frequency and is then amplified, filtered, and digitally divided

to reduce signal noise. Another set of RF filters isolate the tone and is split between Vescent locking circuitry and a phase noise analyzer for data acquisition. The Vescent lockbox utilizes the laser current as a servo for locking and stabilization.

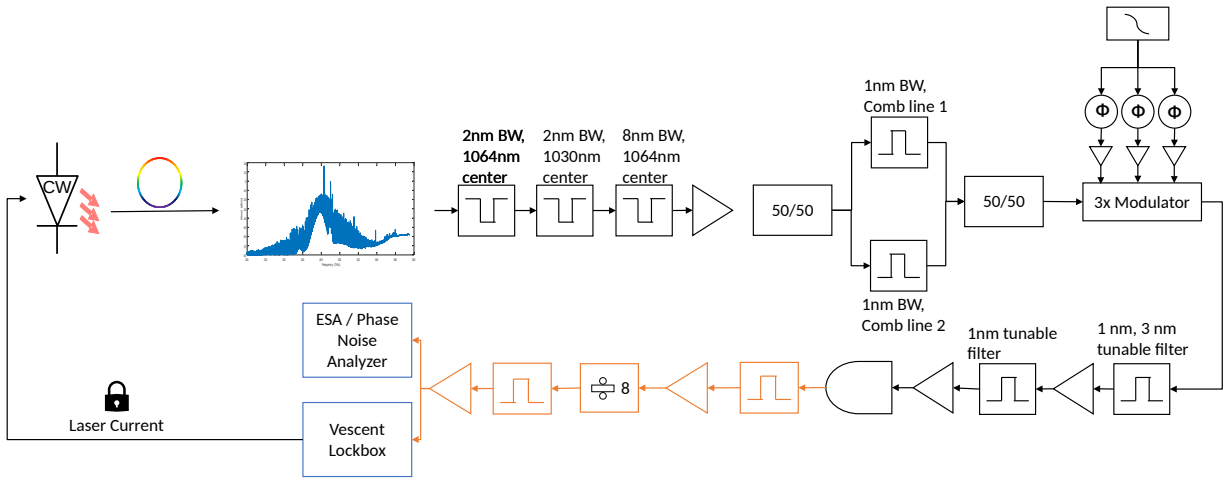

Figure 9| f_{rep} measurement setup. The soliton comb pump lasers are filtered out with bandpass filters and the state is amplified. Two neighboring comb lines are isolated and combined and modulated to generate the 1-THz spanning electro-optic comb. The beat note is filtered and amplified in two successive steps before being photodetected. The RF signal is amplified, divided by 8 and the divided beatnote is filtered, amplified and measured by an electric spectrum analyzer and phase noise analyzer. Stabilization is performed via laser current feedback via a Vescent lockbox.

5 PLATICON GENERATION

5.1 PLATICON BACKGROUND

In a normal-dispersion microresonator, pulse generation has been recently reported to occur with varying modalities such as dark solitons [15, 26], switching waves [57] and platicons [56, 58, 59]. We also report spontaneous platicon comb generation at 19-GHz, stabilized by an avoided

mode crossing and wavelength-dependent quality factor filtering. The mode-locked state is accessed via a polarization-dependent power-kicking method. Multiple bound pulse states of two, three, four, six, seven, and eight pulses are generated with varying relative temporal dispersion. However, due to the high ASE noise of the amplifier, we utilize ultrafast intensity autocorrelation (AC) and frequency-resolved optical gating (FROG) metrology to verify the mode-locked state, and measure the pulse phase noise.

5.2 PLATICON FORMATION

Figure 10a shows the scanning electron micrograph of the silicon nitride microresonator. The device is dispersion managed with seven tapered segments, with widths from 1 to 2.5-μm to tune the dispersion. The simulated GVD is varied from 139-fs^2/mm to -39.7-fs^2/mm, with path-averaged GVD and third order dispersion of 27.9-fs^2/mm and -970.8-fs^3/mm. Figure 10b shows a conceptual diagram of the pulse formation. An avoided mode crossing facilitates spontaneous pulse formation due to the modulated intracavity field background. The microresonator is characterized spectrally by swept-wavelength interferometry, shown in Figure 10c, with a single resonance shown in 10d. The free spectral range is calculated to be 19.7-GHz, with a GVD of 28.2-fs^2/mm, and a loaded quality factor of 1.79-million. When pumped below the pulse-forming threshold, widely-tunable four wave mixing sidebands appear and are able to be controlled via sweeping the laser across the resonance, shown in Figure 10e. The sidebands show 5.2-THz tunability with increasing detuning.

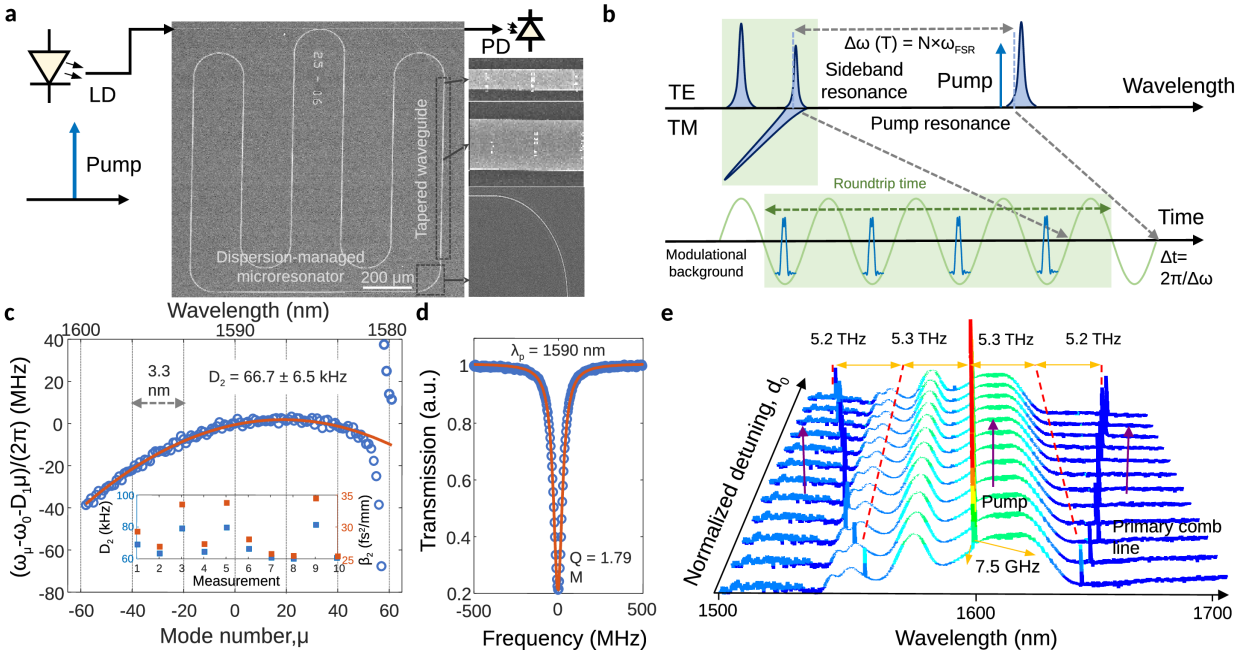

Figure 10| Normal-dispersion microcomb. a, schematic of the generation of the mode-locked platicon frequency comb. b, conceptual illustration of the spontaneous platicon formation via the avoided mode crossing induced modulated background. c, measured integrated dispersion of the microresonator with swept-wavelength interferometry, showing normal dispersion. d, the pumped resonance, showing a Q of 1.79-million. e, spectra of the generated tunable sidebands as a function of pump-resonance detuning, with 5.2-THz tunability.

5.3 MODE-LOCKED STATE GENERATION

To deterministally generate mode-locked pulses, a polarization-dependent power-kicking scheme is implemented to mitigate the thermal effects of the microresonator that reduce the mode-locked state existence range. A polarization modulator is used with bandwidth faster than the thermal response time of the silicon nitride. The pump wavelength is set to near the resonance and instead of detuning into the state normally, the polarization is suddenly changed via an applied voltage to the polarization modulator. This, in conjunction with a polarization beamsplitter, causes the intracavity power to suddenly drop, blue-shifting the resonances and putting the pump

laser into the mode-locked regime of the resonance. First, the thermal dynamics of the resonator are examined by quickly sweeping the pump laser across the resonance at 20-nm/s to measure the hot-cavity transmission, shown in figure 11a. Characteristic mode-locked steps appear with long lifetimes enabled by the avoided mode crossing. Generated comb states are shown in figure 11b with increasing detuning. The optical spectrum has more than 13-THz of -20-dB full-width bandwidth and comb line spacing of 19.7-GHz, matching the free spectral range of the microresonator's fundamental mode. Asymmetry in the spectrum is due to higher-order dispersion terms. Pulse generation and switching is then observed by filtering out the pump laser and performing the fast sweep again, shown in Figure $11c_1$ and $11c_2$. The power is configured to 2-W and the mode-locked pulses are formed with the aforementioned polarization-kicking method. Then, pump power is increased to 2.15-W where multi-pulse states are generated and are able to be annihilated down to a single pulse state with backwards pump detuning. Figure 11d shows the spectral evolution with the scanned pump centered at 1590.11-nm and tuned across the resonance. The comb state evolves through the turing pattern (I), single mode-locked pulse (II), and multi-pulse states (III). The avoided mode crossing acts to disturb the dispersion profile and enable mode-locked pulse formation, similar to a higher-order dispersion term [60]. Figure 11e shows the RF intensity noise of state (III), featuring low intensity noise at the photodetector background noise floor with a clear 19.7-GHz repetition rate tone, indicating pulsed behavior. The center wavelength of the pump is also able to be tuned from 1589 to 1591-nm, shown in Figure 11f, indicating robust pulse stability.

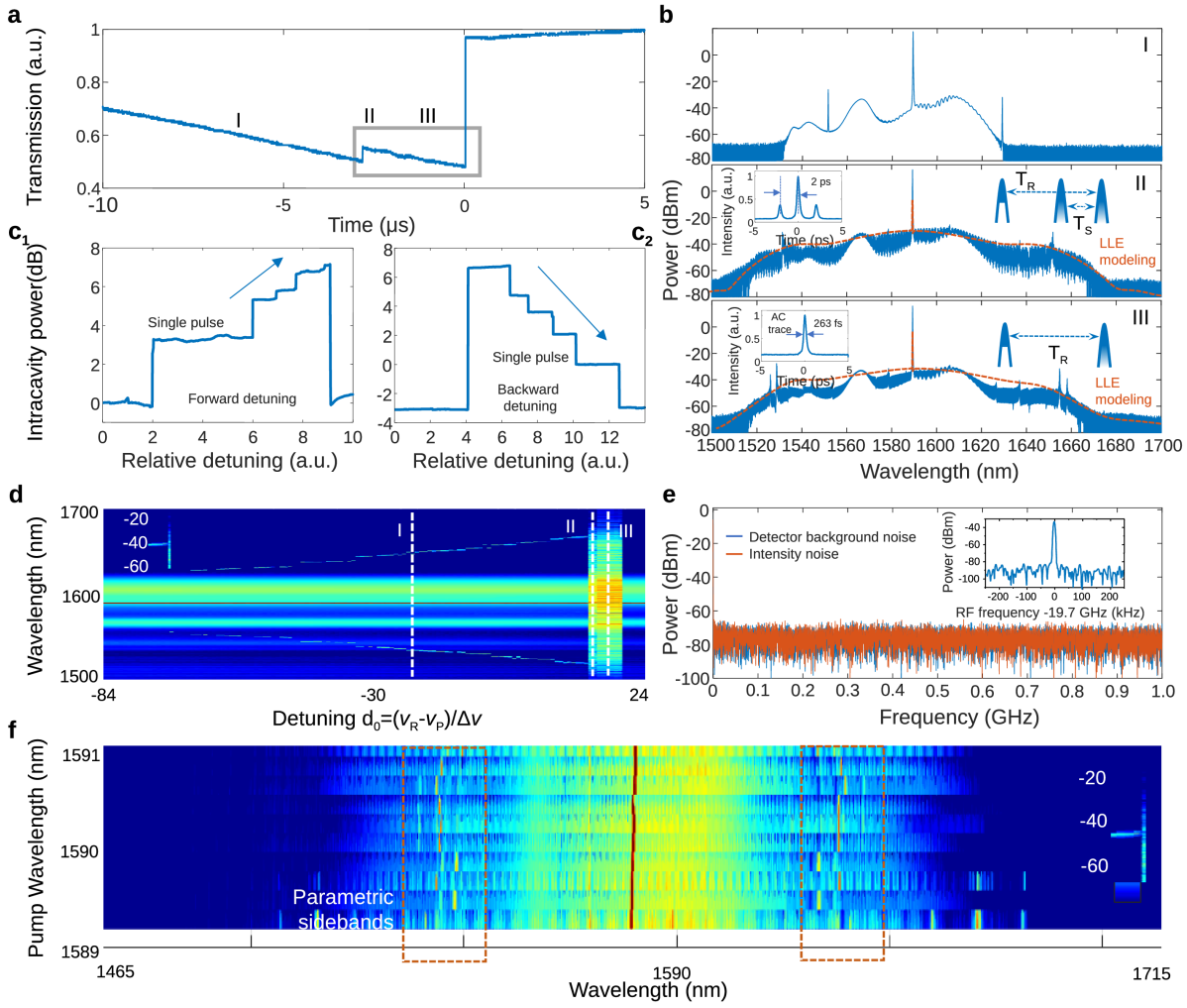

Figure 11| Formation of mode-locked platicon states. a, measured transmission when the pump wavelength is scanned at 20-nm/s across the cavity resonance, with visible pulse steps. b, Frequency comb spectra, showing primary four wave mixing lines (I), double-pulse formation (II) and finally single pulse state (III). Insets are autocorrelation traces of the pulse. Modeled comb spectral envelopes are shown in orange. c_1, c_2, intracavity power evolution of the microresonator when the pump is tuned forward and backward. d, evolution of the comb spectra versus pump detuning. e, RF intensity noise of the mode-locked pulse, showing low background. Inset shows the 19.7-GHz repetition rate beat note. f, mode-locked platicon comb pump wavelength tunability.

5.4 TEMPORAL CHARACTERIZATION

Because the collected spectra have high ASE levels and to understand the temporal properties of the pulses, non-collinear intensity autocorrelation and sub-femtojoule sensitivity FROG measurements are performed [15]. Instead of being a single pulse, platicon bound states are composed of multiple pulses with relative phases separate by some time and can be resolved by the spectral offset of interference fringes relative to the spectral envelope. Figures 12a-d and i-l show several selected optical spectra. The single pulse in the top row has a smooth spectral profile, while the bound-multipulse states have periodically modulated spectral profiles from pulse interference. The modulation period and depth are represented in the optical spectra, and the modulation depth specifically is related to the coherence of the overall pulse across all bound pulses. Comb line spacing of one-FSR is consistent in all optical spectra. Figures 12e-h and m-p show the corresponding autocorrelation traces, indicating mode-locked behavior and revealing the temporal pulse separation. The bound states are separated by 50.7-ps, corresponding tot he round trip time, matching the 19.7-GHz FSR of the microresonator. Regular and irregularly-temporally spaced bound states are observed. Insets show 2D FROG spectrograms with a 16-ps time delay. With a well-defined pump power and detuning, complex bound state patterns can be formed with varying temporal spacing. Specifically, Figure 12i-12l show four, six, seven, and eight tightly phase-locked bound pulses respectively with varying temporal separation. For the case of 8 bound states, there are two pulse bunches with regular temporal separations, which themselves are considered bound pulses linked by the periodically oscillatory tails due to the avoided mode crossing.

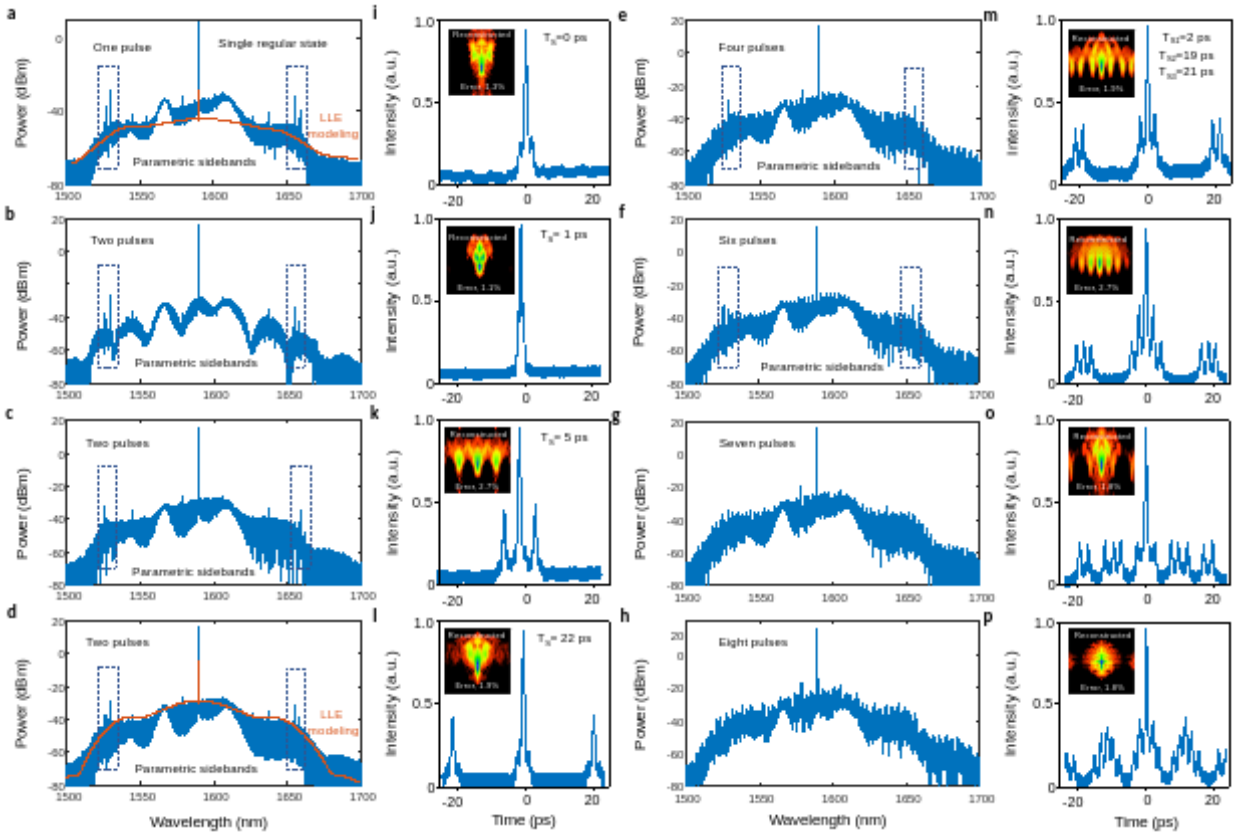

Figure 12| Temporal characteristics of mode-locked states. a-d and i-l, optical spectra of the single, two-pulse, three-pulse, four-pulse, six-pulse, seven-pulse, and eight-pulse bound states. The single pulse is shown in the upper left for comparison. e-h and m-p, intensity autocorrelation traces of their corresponding spectra. Insets: 2D FROG spectrograms, reconstructed via a genetic algorithm.

5.5 REPETITION RATE

The mode-locked pulse generation and characterization setup is shown in Figure 13a. The pumping setup is similar to the previously-mentioned configuration, with modifications to the data collection for more thorough analysis. The total transmission loss of the microresonator is lower than 6-dB. Because the 19.7-GHz is directly detectable with a 20-GHz InGaAs photodetector, the repetition rate and phase noise can be directly characterized in the K-band.

Figure 13b shows measured single-sideband phase noise at various mode-locked state, with corresponding RF beatnoes after frequency division in the insets. After amplification to the same power level for all mode-locked states, the repetition rate is also measured and characterized. The RF signal is clean over a 5-MHz spectral range with a signal-to-noise ratio of more than 70-dB. This also confirms mode-locking behavior, with performance similar to that of current K-band microwave oscillators. The phase noise of the reptition rate is found to be approximately -90-dBc/Hz at the 10-kHz Fourier offset frequency. The phase noise spectra all show a power-law slope of 30-dB/decade from 10-Hz to 40-Khz caused by the free-running pump-resonance detuning instability [61]. Peaks in the phase noise from 10 to 70-kHz are caused by the amplification. The light gray curve shows the measured relative intensity noise of the comb state. Other similar oscillators are shown in Figure 13b for comparison. The single-pulse microcombhas better phase noise than the multi-pulse bound states at offset frequencies lower than 10-kHz. Noise degradation is attributed to spectral interference and the pump-resonance detuning noise. Beyond 10-kHz, the amplifier sponatneous emission limits at -116-dBc/Hz for the 1-MHz Fourier offset frequency, related to the incident optical power. 6-dB degradation is also observed as pulse number increases.

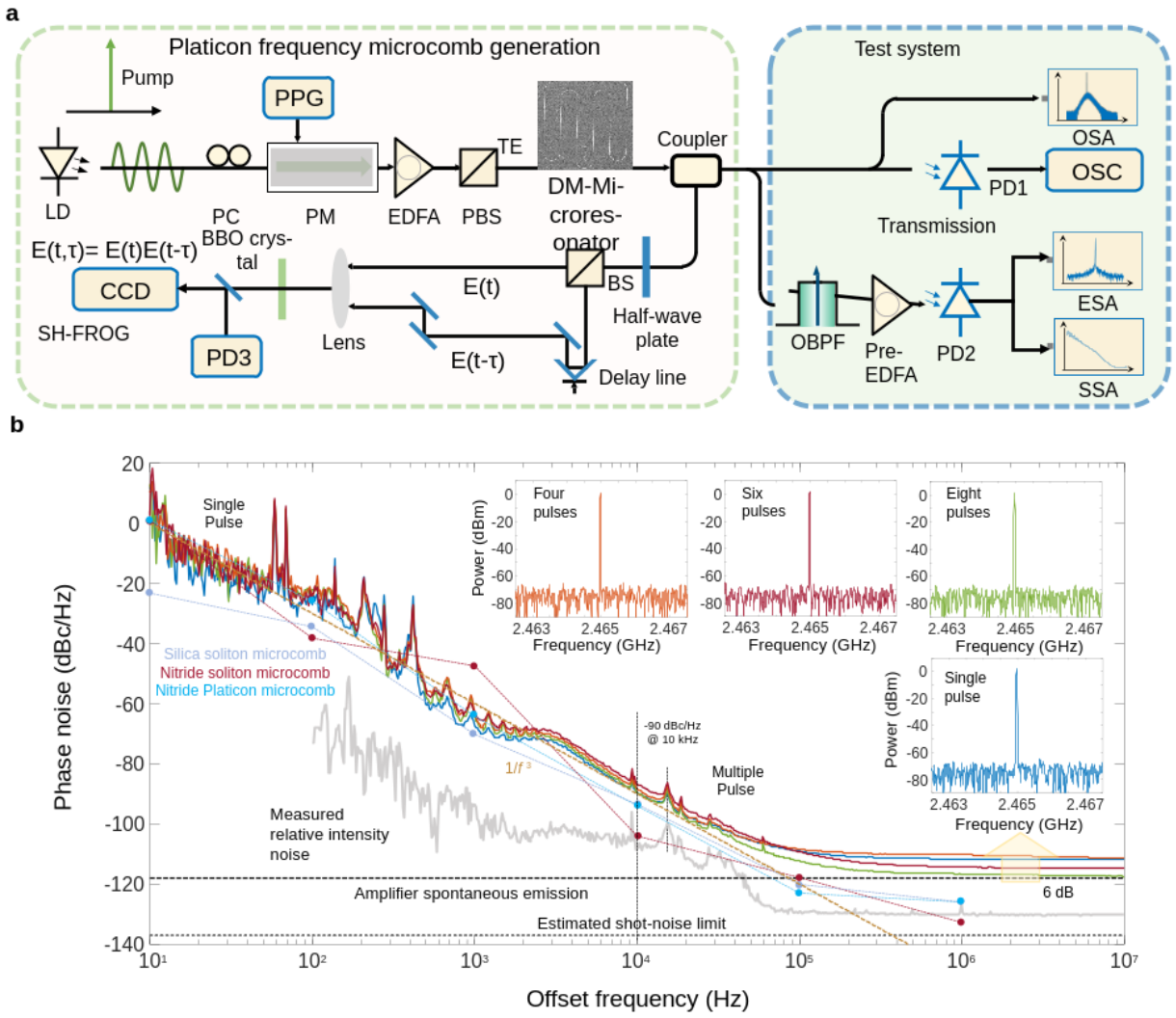

Figure 13| Repetition-rate characterization. A, experimental setup for monitoring optical transmission, comb state, and RF spectra. LD: laser diode; PC: polarization controller; PM; polarization modulator; PPG: pulse pattern generator; EDFA: erbium-doped fiber amplifier; PBS: polarization beam splitter; OSA: optical spectrum analyzer; OSC: oscilloscope; ESA: electrical spectrum analyzer; SSA: signal source analyzer; PD: photodetector; OBPF: optical bandpass filter; BS: beam splitter; BBO: β-barium borate; CCD: charge-coupled device. B, single-sideband phase noise spectra of the 19.7-GHz repetition rate beat notes for various mode-

locked states. Relative intensity noise is shown as the gray curve. Insets: corresponding repetition-rate beat note spectra after 8x frequency division.

6 OCT BACKGROUND AND PREVIOUS WORK

6.1 TRADITIONAL OCT

Optical coherence tomography (OCT), developed in 1991 by Huang et. al., is a noninvasive cross-sectional tissue imaging technique widely used in the field of ophthalmology [41-43], intravascular imaging [44], disease screening [45, 46], and brain imaging [47]. Fundamentally, OCT works by utilizing low-coherence interferometry from which a single slice of the tissue can be imaged, analogous to ultrasonic pulse-echo imaging [48]. OCT can be performed in both the time domain (TD-OCT) with a broadband light source where the reference arm path length is modulated and data is collected in one channel over time or in the frequency domain (FD-OCT) where a broadband light source employs light frequencies rather than time delays to form the interferogram, which then can be passed through a Fourier transform to obtain spatial information (SD-OCT), with a further variation that uses a narrow light source that sweeps across a band of wavelengths, marking time delays and detecting them via interferograms (SS-OCT) [48, 49]. The focus of this work is SD-OCT. Stacking multiple individual “A-scans” together by sweeping the targeting point creates a 2D image, called a “B-scan” [48, 49]. This is realized by scanning over one of the lateral dimensions to create a 2D reflection map which represents the internal structure of the sample [49]. FD-OCT provides detection down to the shot noise level and is generally advantageous over TD-OCT in terms of acquisition speed and sensitivity and commonly uses a SLD as the light source [49].

Experimentally, SD-OCT is realized as a fiber-optic Michelson interferometer illuminated by broadband, low-coherence light where the sample to be imaged is placed in one arm of the interferometer [49]. Reflections from the sample interfere with the reference arm and the interferometric signal is recorded. The beam can be scanned across the tissue using motorized mirrors to in one axis to obtain B-scans and two axes to obtain volumetric scans [49]. A key consideration of SD-OCT is the extremely high detection sensitivity – a 20-uW incident source can provide sensitivity of 10-fW with optical heterodyne detection [48]. This combined with its high resolution lends SD-OCT to detection and aid-of-diagnosis of diseases such as glaucoma, macular degeneration, and macular edema [48, 49]. Optical properties of structures, such as birefringence, can help identify specific tissue within the eye or other targets, given the structure of the tissue is known, and the wavelength independence of the method allows measurement of other spectral properties such as oxygenation of hemoglobin, hydration, and chromophore content [48].

6.2 OCT WITH DISCRETE LIGHT SOURCE

With SD-OCT, limitations in imaging range occur due to the finite resolution of the spectrometer and a depth-dependent sensitivity drop is observed [49, 50]. While some methods have been proposed to circumvent the sensitivity drop-off, they tend to decrease system acquisition speed or require additional processing [49, 50]. In 2008, Bajraszewski et. al. proposed employing an optical frequency comb to reduce the depth-dependent drop of sensitivity and more flexible variation of measurement depth without modifying the underlying SD-OCT structure in addition to avoiding wavelength-to-frequency rescaling due to the equally distant optical frequencies [50].

In the situation of a passive optical frequency comb generator made of a broadband light source and Fabry-Perot filter, the real component of the interference signal $I(k)$ is multiplied by the transmission function of the filter T_{Fp}, which can be written as a convolved Cauchy/Lorentz distribution and Dirac Delta comb, $D_{\pi}(k)$:

$$I_{OFC}(k)=T_{FP}(k)\,I(k) \tag{5}$$

$$T_{FP}=\frac{\pi T^2}{d\left(1-R^2\right)}L(k;\gamma)\otimes D_{\frac{\pi}{d}}(k) \tag{6}$$

where T and R are the transmission and reflection coefficients of the Fabry-Perot filter surfaces respectively, $\gamma=(2d)^{-1}\ln(R)$, d is the distance between the filter surfaces, and $L(k;\gamma)$ is the Cauchy/Lorentz distribution function [50]. Overall, a total real interference signal of

$$I_{OFC}(k)=\frac{\pi T^2}{d\left(1-R^2\right)}L(k;\gamma)\otimes D_{\frac{\pi}{d}}(k)I(k) \tag{7}$$

is found and the Fourier transform is calculated to be

$$FT\left\{I_{OFC}(k)\right\}=G^{OFC}(z)=\frac{\sqrt{2\pi}T^2}{1-R^2}\exp\left(\frac{\pi}{d}\ln(R)|z|\right)D_{2d}(z)\otimes g(z) \tag{8}$$

where g(z) is the Fourier transform of $I(k)$ [50]. From this equation the periodic structure of the tomogram in depth arises if the frequency or time difference is sampled by the detector and is observable in frequency comb OCT tomograms where this condition is met [50, 51]. This structure can be taken advantage of by ensuring each comb line illuminates only one pixel on the CCD and the line bandwidth of the comb is much smaller than a single pixel's spectral range, reducing interpixel crosstalk and SNR falloff [50].

7 OCT IMAGING AND RESULTS

7.1 CHOOSING A COMB STATE

Crucial to high fidelity frequency comb OCT imaging is choosing the correct comb state. All comb lines should be of approximately the same power for as large of a spectral bandwidth as possible to reduce the need for post-processing [51]. Any set of comb lines that are significantly higher power than the surrounding lines will add noise in the form of bright or saturating pixels or scan lines, degrading the OCT tomogram [52]. Therefore, it is desirable for the comb spectra to be as smooth and broad as possible to optimize the initial interferogram. Comb bandwidth is vitally important to the axial resolution, calculated by the formula:

$$\Delta z = \frac{2\ln(2)}{\pi}\frac{\lambda_c^2}{\Delta\lambda_{\mathrm{BW}}} \tag{9}$$

where λ_c is the light source center wavelength and $\Delta\lambda_{BW}$ represents the light source bandwidth [52]. The axial resolution is inversely proportional to the comb bandwidth and can be chosen via proper dispersion engineering. Maximum imaging depth is calculated via the relation:

$$z_{max} = \frac{\lambda_c^2}{4\delta_s} \tag{10}$$

where δ_s is the spectrometer sampling interval [52]. In the case that the spectrometer's sampling interval is perfectly matched to the comb line spacing, the imaging depth is inversely proportional to the comb FSR. Therefore, it is advantageous to design a microresonator with a smaller FSR for improved imaging depth. However, as FSR decreases, the spectral bandwidth of the resultant comb decreases resulting in a tradeoff between the imaging depth and axial resolution, influenced by comb bandwidth, the FSR of the comb, and comb spectrum

smoothness. Based on these factors and the comb states generated, a comb with 95-GHz FSR is chosen to optimize tomogram clarity and resolution without sacrificing too much imaging depth.

A choice between a chaotic combs and DKS state should also be considered. Whereas the chaotic state can have a wider flat peak due to a less envelope-constrictive phase matching condition, additional comb line amplitude noise is introduced serving to decrease the tomogram SNR [51, 52]. Conversely, the dispersive Kerr solution adheres to an envelope following a hyperbolic secant and will not necessarily have the same 3-dB bandwidth as a chaotic comb state but will have much less individual comb line amplitude fluctuation [53]. A chaotic comb state is chosen because by taking multiple acquisitions, averaging several measurements greatly reduces the effect of individual comb line fluctuation while accessing bandwidth higher than that of a soliton of the same FSR.

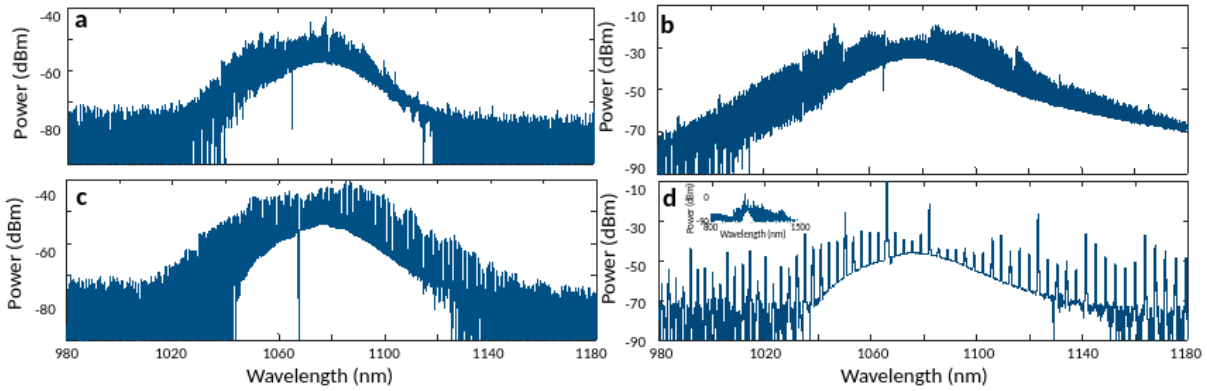

Figure 14| Selected OCT frequency comb candidates. (a) Comb spectra of a 54-GHz microcomb. Multiple envelope abberations and narrow bandwidth of only approximately 100-nm makes this a poor option for OCT imaging. (b) Comb spectra of a 95-GHz microcomb. The presence of only a few aberrations and a broader spectral bandwidth makes this a stronger option for OCT imaging. (c) Comb spectra of a 200-GHz microcomb. Although the comb is very spectrally smooth and has a bandwidth of approximately 300-nm, the FSR relegates this comb

state to only being useful, providing very low imaging depth. (d) Comb spectra of a 1-THz microcomb. The FSR of this microcomb is too large for meaningful OCT imaging surface tissue. Inset: Spectrum of entire 1-THz comb, spanning 700-nm.

7.2 OCT IMAGING RESULTS

Frequency comb OCT tomograms of a stack of scotch tape, an orange peel, a porcine retina, and a strawberry are taken with an A-scan rate of 76-kHz. B-scans for all tomograms except the strawberry and porcine retina are acquired in sets of 10, passed through a series of post-processing steps discussed in Section 7, and then the resulting tomograms averaged as the final step to increase SNR [54]. A stack of 6 layers of Scotch tape is imaged using an SLD and a frequency comb for direct comparison of each light source with all other experimental variables constant except for the averaging of the frequency comb-lit tomogram. Qualitatively, both the frequency comb tomogram and the SLD tomogram look similar with all features of the tape stack present. Edges between each tape layer are clear and the painter's tape layer on the bottom of the stack is distinct. The interferogram for the SLD lit source has a smooth, gaussian envelope over multiple B-scans and leads to a clean Fourier transform to view the image. The interferogram for the frequency comb after post-processing is also roughly gaussian but is spurious and not as smooth with gaps within the interferogram, a result of the aberrations of the comb state envelope. Because multiple scans are averaged together, the tomogram results are still qualitatively on par with that of the SLD-lit tomogram.

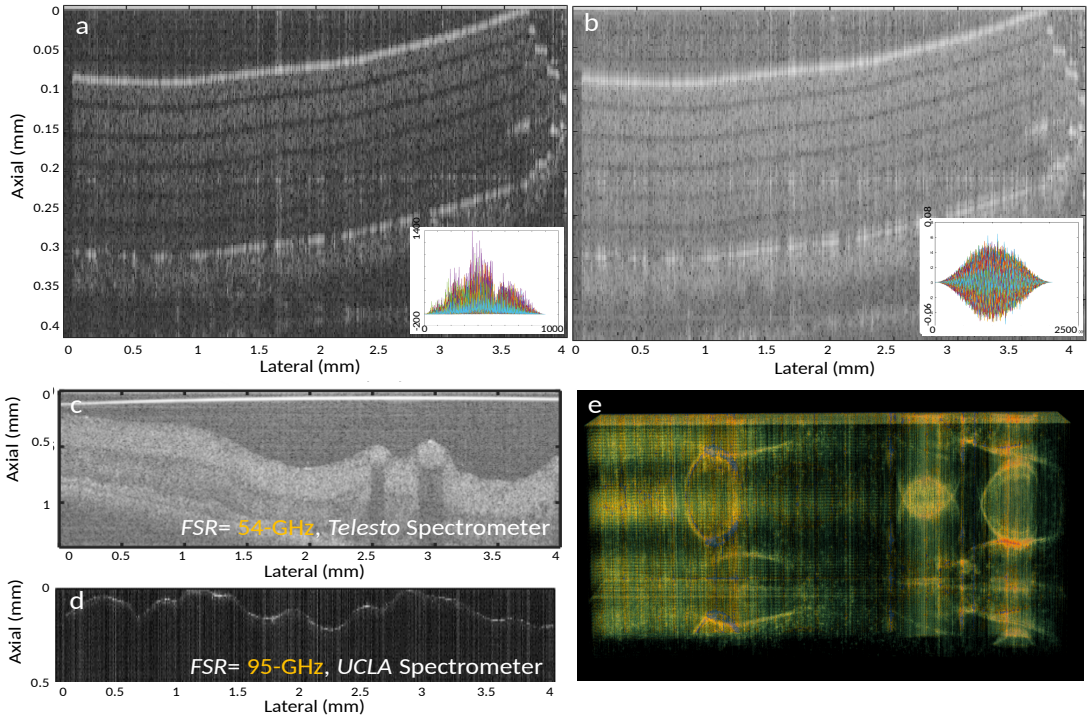

Figure 15| OCT imaging results. (a) OCT image utilizing a 95-GHz frequency comb and UCLA spectrometer. All layers of the tape stack are clearly visible and very little distortion is present. Inset: overlaid interferograms resultant in the tape stack image. The gaussian envelope is visible, although distorted due to noise from the chaotic comb state and avoided mode crossings. (b) OCT image utilizing an SLD and UCLA spectrometer. All layers of the tape stack are visible and little distortion is present. Inset: overlaid interferograms resulting in the tape stack image. The gaussian envelope is clearly defined and little distortion visible. (c) OCT image of a pig retina utilizing a 54-GHz frequency comb and Telesto spectrometer. Two blood vessels are visible at 2.5mm and 3mm in the lateral dimension. Due to the configuration of the Telesto spectrometer, some SLD light is included in this tomogram. (d) OCT image of an orange peel utilizing a 95-GHz frequency comb and UCLA spectrometer. Surface structure is visible and well-defined, with bright spots residing on the surface due to oils or other liquids from the peel. No light from the SLD is present in any tomograms using the UCLA spectrometer. (e).

Volume OCT scan of a strawberry using 95-GHz comb and the UCLA spectrometer. Surface structure of the strawberry is visible and strawberry seeds can clearly be observed. The volume can be observed to mirror itself, indicative of a discrete OCT light source.

A pig retina is imaged for demonstration using tissue. A 54-GHz comb and the Telesto spectrometer are utilized for this measurement. Tissue structure is visible and blood vessels can also be seen with high contrast. It is important to note that the optical path of the Telesto includes some SLD light whenever its spectrometer is used. An orange peel is also chosen for a target with less regular structure. The contours of the surface of the peel and areas where oils from the peel reside on the peel surface are clearly visible, identifiable by the localized bright spots. More visual artifacts exist in this scan in the form of vertical lines, manifesting from comb line noise in the comb state. These could be removed by utilizing a more stable comb state. Finally, a volumetric scan is performed on a strawberry. Whereas with the other B-scans only show one period for clarity, the ambiguity range and subsampling repetition are included here. Surface features are identifiable, such as strawberry seeds, and the ambiguity range and repetition inherent with discrete light source OCT is obvious. More clear images can be obtained by optimizing the distance between the target and the objective to keep the target completely in frame and out of the ambiguity region.

7.3 AXIAL RESOLUTION MEASUREMENT

To ascertain the axial resolution of the OCT system, take the tomogram of a reflector is taken and the resulting gaussian peak is fit; by taking the full-width half-maximum of the resulting fit, the axial resolution utilizing the specific comb state can be calculated [54]. To take this measurement, a beam splitter is utilized as a reflector rather than a mirror because the line scan camera used in the spectrometer saturates when using a mirror. The effective axial

resolution is calculated as 5.65±1.7-um, near the theoretical limit of 6.2-um, shown in tabular form in Table 1. The axial resolution is called effective as the fitting is performed post-processing.

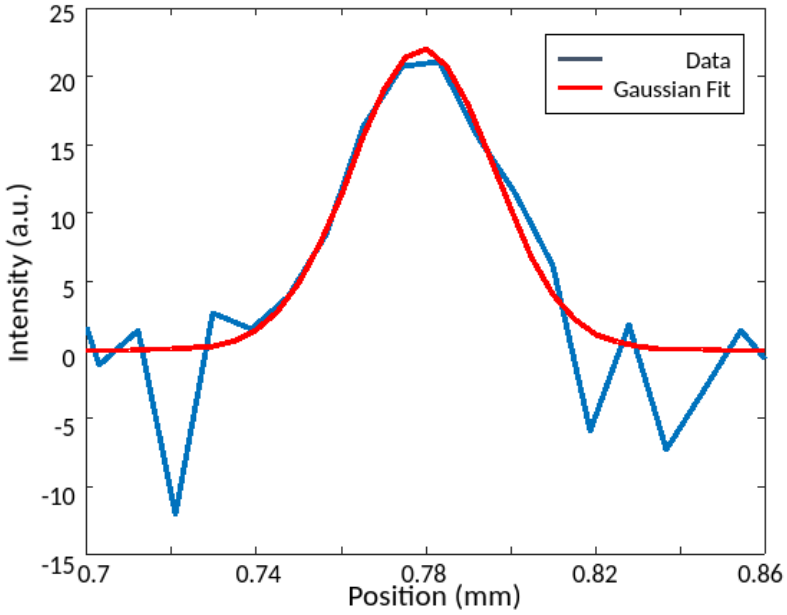

Figure 16| Axial resolution measurement. Axial resolution measurement of OCT system utilizing 100GHz frequency comb with an axial resolution of 5.65±1.7-µm.

Spectral Bandwidth Full Width Half Maximum	**Axial Resolution Central wavelength = 1064 nm**	
	in air	in tissue (n = 1.4)
30 nm	27 µm	12 µm
80 nm	**6.2 µm**	**4.5 µm**
100 nm	5.0 µm	3.5 µm
200 nm	2.5 µm	1.8 µm
300 nm	1.6 µm	1.1 µm

Table 1| Spectral bandwidth and ideal axial resolution. This work is in bold.

Frequency Comb Free Spectral Range	Imaging Depth a	
	in air	in tissue (n = 1.4)
1000 GHz	0.075 mm	0.05 mm
200 GHz	0.37 mm	0.27 mm
95 GHz	0.94 mm	0.67 mm
54 GHz	**1.4 mm**	**1.0 mm**
27 GHz	2.7 mm	1.9 mm

Table 2| Comb FSR and ideal imaging depths. This work is in bold.

8 FREQUENCY COMB OCT POST PROCESSING

8.1 PHASE CALIBRATION

Before any rigorous post-processing is applied to the collected interferogram, a calibration must be performed to correct nonlinear mapping of the spectrometer grating as well as wavevector phase variation correction from residual dispersion in the reference and target arms [54]. The detected spectrum for a single reflector with reflectivity r_s is defined as

$$I_{det}(k)=\frac{1}{4}I_{source}(k)\left(1+r_s+2\sqrt{r_s}\cos\left(2k\Delta z+\phi_d(k)\right)\right) \tag{11}$$

By taking two measurements slightly separated from one another of the simple reflector, the phase component is extracted using the Hilbert transform and can therefore determine the wavenumber correction vector and residual dispersion using:

$$\phi_1(n)=2k\left(z_1-z_s\right)+\phi_d \tag{12}$$

$$\phi_2(n)=2k\left(z_2-z_s\right)+\phi_d \tag{13}$$

$$\Delta\phi(n)=\phi_1(n)-\phi_2(n) \tag{14}$$

where k is the wavevector, z_1, z_2, z_s are the first, second, and starting distances, respectively, and ϕ_d is the correction [54]. This correction is applied in the processing stack to improve the tomogram signal.

8.2 PROCESSING STACK

Several processing steps are applied to extract the tomograms from the interferograms measured by the frequency comb OCT and improve their quality [54]. First, background noise is subtracted followed by applying a moving average gaussian filter to the interferogram to spectrally form the data closer to a gaussian function [55]. The width of the gaussian window is a key parameter to achieving a clear OCT result and is a degree of freedom of which is tuned to find the best-fitting gaussian function. Next, apodization in the form of a Hann window is applied to preserve the bandwidth of the interferogram and drive down the noise floor [54]. Use of a Blackman window instead of a Hann window demonstrates little qualitative improvement, indicating bandwidth is not apodization limited and preserved [54]. Phase corrections calculated during the calibration step are applied as a spline interpolation and then the Fast Fourier Transform is performed to reach the final tomogram [54, 55]. To improve the SNR of the resulting image, multiple B-scans in the same configuration and target position are averaged to reduce the effect of spurious, saturated A-scans that appear as vertical artifacts. This step is necessary due to the chaotic nature of the comb state and could be bypassed if a soliton was used instead with the additional boon of improving imaging speed.

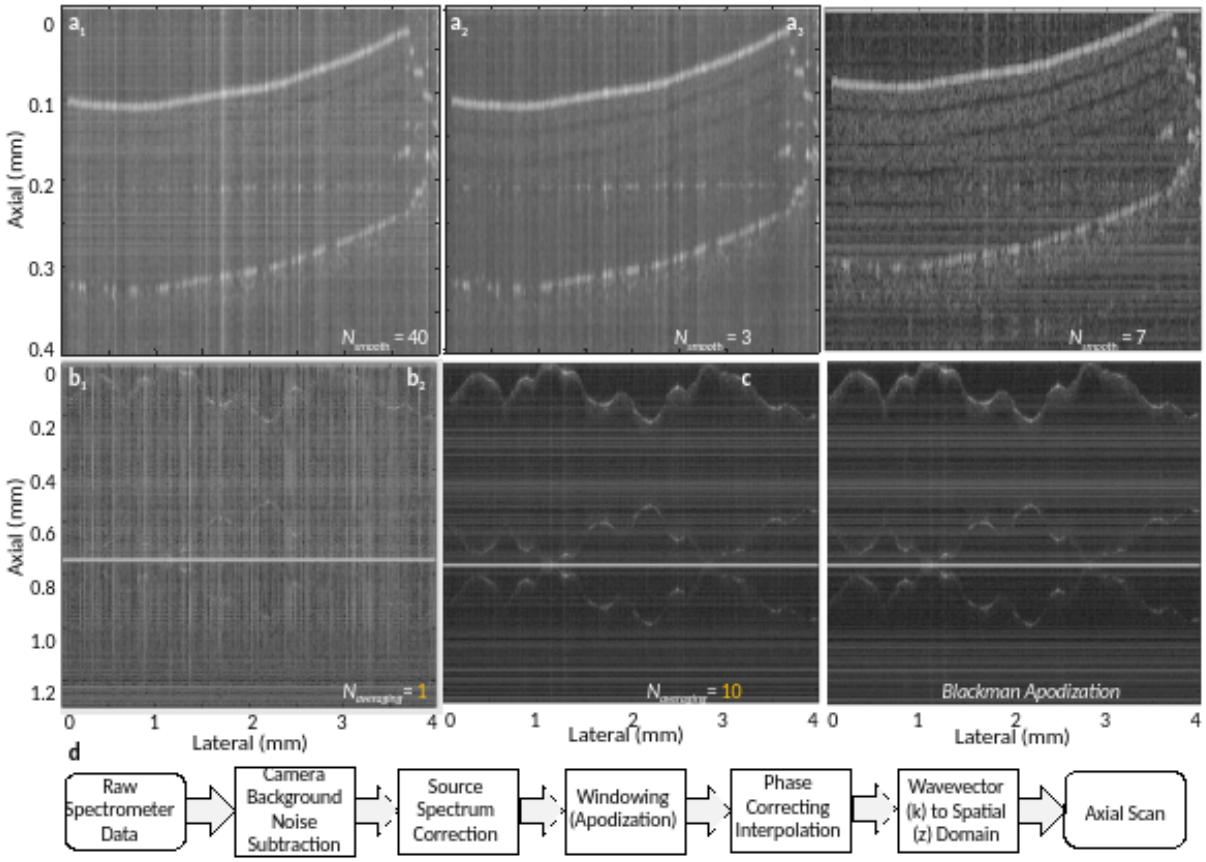

Figure 17| OCT processing stack. (a1) Tape stack with Gaussian window width of 40. The high sliding window value causes the internal structure of the tape stack to be washed out. (a2) Tape stack with Gaussian window width of 3. The small window value reveals some internal details but most of the tape layers are not visible. (a3) Tape stack with Gaussian window width of 7. This is well tuned to reveal the entirety of the internal structure. (b1) Orange peel, no averaging. Without averaging over multiple OCT scans, the comb line intensity noise overwhelms the image and much of the detail is lost. (b2) Orange peel averaged over 10 OCT scans. Much of the comb line intensity noise averages out and the overall clarity of the image increases. (c) Blackman apodization applied to b2 instead of Hann. Comparison with b2 shows very few differences, indicating bandwidth is well-preserved. (d). Flowchart of the post-

processing steps. Data undergoes background subtraction before being spectrally corrected with a gaussian. Data then passes through apodization to improve bandwidth before undergoing phase correcting interpolation and transformed to spatial coordinates via Fourier transform.

9 MEASUREMENT DETAILS

9.1 DETAILS OF THE MEASUREMENT SETUP

The OCT setup is shown in Figure 14. A Sacher Lasertechnik 1064nm laser is controlled with a PC to pump the microresonator after amplification with a YDFA at 1W. Light is coupled to the chip via lensed fibers. The output of the microresonator then has 1% tapped to monitor power and the comb state for comb generation and optimization while the other 99% continues through a circulator and fiber Bragg grating to filter the pump to avoid damaging or saturating the spectrometer. The comb then passes through a circulator to the OCT optics and probe – a Thorlabs Telesto II unit is used. The back-reflected interferogram then travels back through the circulator to either the Telesto OCT Base Unit which contains the Telesto internal spectrometer, or to the UCLA homemade spectrometer. When using the UCLA spectrometer, a trigger signal is sent the Telesto to control the internal mirrors to scan over the target – Telesto software allows external control of this trigger signal, which is generated in custom-written software.

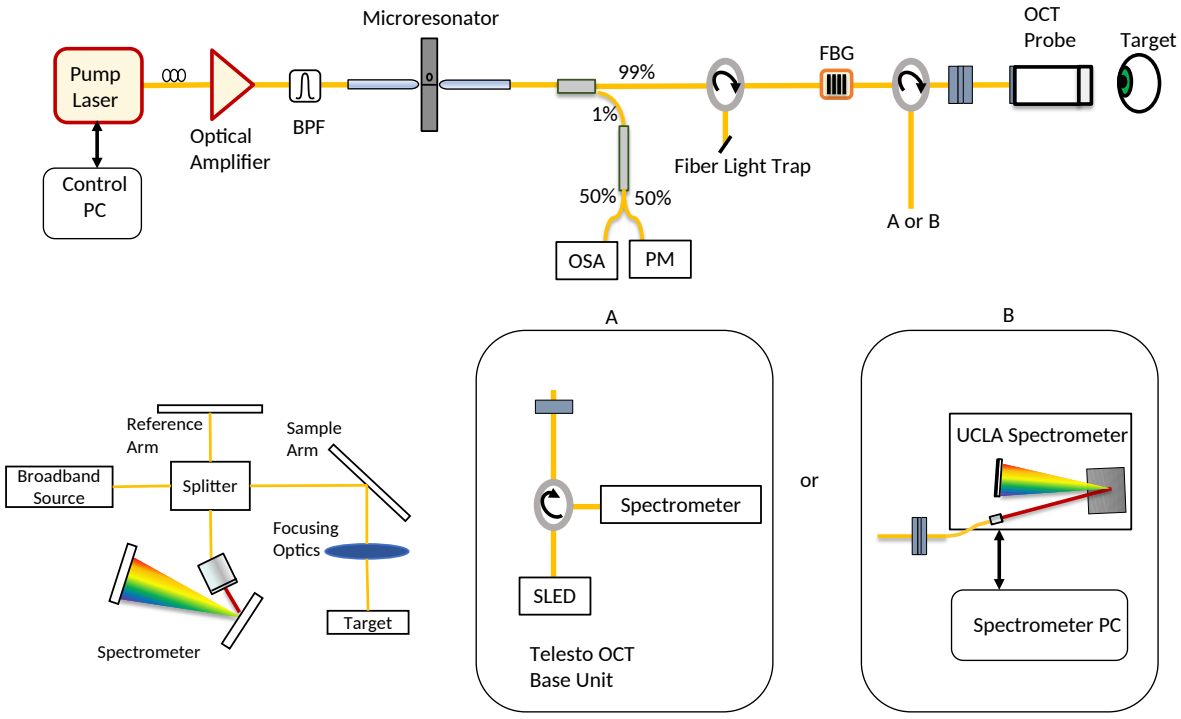

Figure 18| OCT measurement setup. Diagram of the OCT system. The sample is placed in one arm of the Michaelson interferometer and generates the interferogram and is sent to a spectrometer and maps the wavelengths to pixels. The implementation utilizes a Telesto II unit for the interferometer and focusing optics and allows use of either the built-in spectrometer or the custom-built UCLA spectrometer.

9.2 DETAILS OF THE SPECTROMETER

The Telesto II spectrometer has a bandwidth of approximately 62-nm and limits the resolvable axial resolution, instead designing for a larger imaging depth of 10-mm. As an alternative, a new spectrometer is designed with a goal bandwidth of 200-nm centered at 1080-nm that has an imaging depth of 1.5-mm. A Thorlabs RC08APC-P01 collimator, a Wasatch transmission grating with 1100-lines/mm for a designed wavelength of 1087-nm, and 4 stock lens custom-modified Cooke Triplet for the object lens are used. A Xenics Lynx-R line scan

camera controlled by the Euresys Grablink Full 1622 is used to grab frames of the spectrometer. The grating equation to determines $\beta_{min}, \beta_0, \beta_{max}$, the dispersed angles,

$$\sin(\alpha)+\frac{\lambda}{\Delta}=\sin(\beta) \tag{15}$$

where α is the Littrow angle defined by the grating and β_{min}, β_{max} are determined by the required wavelength span of the spectrometer. To achieve the desired spectral resolution, it's required that the beam must illuminate at least N lines of the grating which determines the beam illumination diameter, and an approximate requirement on focal length determined by the camera sensor size is set,

$$N_{min}=\frac{\lambda_{max}}{\delta\lambda} \tag{16}$$

$$D=N_{min}\Delta\cos(\alpha) \tag{17}$$

$$f \quad \frac{\delta p\, N_{pixels}}{\Delta\beta} \tag{18}$$

A 4-lens Cooke Triplet that is modified for stock lenses is simulated, ensuring the RMS spot size stays below the horizontal pixel pitch which is the dispersive dimension [54]. The spectrometer is aligned and calibrated using a 200-GHz frequency comb.

10 FUTURE WORK

Regarding OCT, a 95-GHz FSR comb is chosen because the available 54-GHz combs had too many aberrations in their spectra; using devices with a mode filtering section would reduce the number of mode interactions and smooth the spectral envelope, leading to deeper imaging depth. In addition, the development of Nyquist square Kerr frequency combs or

platicons in normal dispersion devices lends itself to potential OCT application due to their generally square shape and broad phase matching in the center of the comb [56]. Another potential comb source could be zero-dispersion Kerr solitons, which can achieve incredibly wide bandwidths of more than 440-nm with a 27.8-GHz FSR, circumventing the tradeoff between imaging depth and axial resolution [57]. Lastly, the 1-THz soliton combs that span nearly an octave can be used in conjunction with the electro-optic combs to bypass the axial resolution and imaging depth tradeoff. Further work towards designing normal dispersion microresonators for platicon comb design and dynamics analysis are planned.

11 CONCLUSION

In conclusion, 1-um wavelength, 1-THz frequency combs are simulated, designed, and measured. Both the repetition rate and center offset frequency are calculated and control over f_{ceo} is demonstrated. The 1-THz soliton state reaches a phase noise of -130dBc/Hz with the potential to decrease further with reduced electronic division for improved locking sensitivity.

Additionally, optical coherence tomography with a 1um frequency comb is demonstrated with competitive axial resolution and image clarity. By taking advantage of the Kerr frequency comb's unique position as a small, lightweight, low power, broad and discrete light source, the comb-driven OCT system is an improvement over traditional SLD-based OCT systems. Through utilization of microresonators with lower FSRs, imaging depth can be pushed further and surpass SLDs as the light source of choice.

12 REFERENCES

[1] R. Holzwarth, Th. Udem, T. W. Hänsch, J. C. Knight, W. J. Wadsworth, and P. St. J. Russell, "Optical Frequency Synthesizer for Precision Spectroscopy," *Phys. Rev. Lett.* **85**, 2264–2267 (2000)

[2] P. Del'Haye, A. Schliesser, O. Arcizet, T. Wilken, R. Holzwarth, and T. J. Kippenberg, "Optical frequency comb generation from a monolithic microresonator," *Nature* **450,** 7173 (2007)

[3] T. Herr, V. Brasch, J. D. Jost, C. Y. Wang, N. M. Kondratiev, M. L. Gorodetsky, and T. J. Kippenberg, "Temporal solitons in optical microresonators," *Nature Photon* **8**, 145–152 (2014).

[4] H. Zhou, Y. Geng, W. Cui, S. W. Huang, Q. Zhou, K. Qiu, and C. W. Wong, "Soliton bursts and deterministic dissipative Kerr soliton generation in auxiliary-assisted microcavities," *Light Sci Appl* **8**, 50 (2019).

[5] P. Delva, J. Lodewyck, S. Bilicki, E. Bookjans, G. Vallet, R. Le Targat, P. E. Pottie, C. Guerlin, F. Meynadier, C. Le Poncin-Lafitte, O. Lopez, A. Amy-Klein, W. K. Lee, N. Quintin, C. Lisdat, A. Al-Masoudi, S. Dörscher, C. Grebing, G. Grosche, A. Kuhl, S. Raupach, U. Sterr, I. R. Hill, R. Hobson, W. Bowden, J. Kronjager, G. Marra, A. Rolland, F. N. Baynes, H. S. Margolis, and P. Gill. "Test of Special Relativity Using a Fiber Network of Optical Clocks," *Phys. Rev. Lett.* **118**, 221102 (2017).

[6] Y. S. Jang, H. Liu, J. Yang, M. Yu, D. L. Kwong, and C. W. Wong, "Nanometric Precision Distance Metrology via Hybrid Spectrally Resolved and Homodyne Interferometry in a Single Soliton Frequency Microcomb," *Phys. Rev. Lett.* **126**, 023903 (2021).

[7] S. A. Diddams, A. Bartels, T. M. Raymond, C. W. Oates, S. Bize, E. A. Curtis, J. C. Bergquist, and L. Hollberg, “Design and control of femtosecond lasers for optical clocks and the synthesis of low-noise optical and microwave signals,” *IEEE Journal of Selected Topics in Quantum Electronics* **9**, 1072–1080 (2003).

[8] K. Minoshima, and H. Matsumoto, “High-accuracy measurement of 240-m distance in an optical tunnel by use of a compact femtosecond laser,” *Appl Opt* **39**, 5512–5517 (2000).

[9] A. S. Kowligy, H. Timmers, A. J. Lind, U. Elu, F. C. Cruz, P. G. Schunemann, J. Biegert, and S. A. Diddams, “Infrared electric field sampled frequency comb spectroscopy,” *Science Advances* **5** (2019).

[10] 1. G. Ycas, F. R. Giorgetta, E. Baumann, I. Coddington, D. Herman, S. A. Diddams, and N. R. Newbury, “High-coherence mid-infrared dual-comb spectroscopy spanning 2.6 to 5.2 μm,” *Nature Photon* **12**, 202–208 (2018).

[11] X. Ji, X. Yao, A. Klenner, Y. Gan, A. L. Gaeta, C. P. Hendon, and M. Lipson, “Chip-based frequency comb sources for optical coherence tomography,” *Opt. Express* **27**, 19896–19905 (2019)

[12] P. Del’Haye, A. Schliesser, O. Arcizet, T. Wilken, R. Holzwarth, and T. J. Kippenberg, “Optical frequency comb generation from a monolithic microresonator,” *Nature* **450**, 1214–1217 (2007).

[13] T. J. Kippenberg, S. M. Spillane, and K. J. Vahala, “Kerr nonlinearity optical parametric oscillation in an ultrahigh-Q toroid microcavity,” Phys. Rev. *Lett*. **93**, 083904 (2004).

[14] M.-G. Suh, Q.-F. Yang, K. Y. Yang, X. Yi, and K. J. Vahala, “Microresonator soliton dual-comb spectroscopy,” *Science* **354**, 600–603 (2016).

[15] S.-W. Huang, H. Zhou, J. Yang, J. F. McMillan, A. Matsko, M. Yu, D.-L. Kwong, L. Maleki, and C. W. Wong, “Mode-Locked Ultrashort Pulse Generation from On-Chip Normal Dispersion Microresonators,” *Phys. Rev. Lett*. **114**, 053901 (2015)

[16] Y. Okawachi, K. Saha, J. S. Levy, Y. H. Wen, M. Lipson, and A. L. Gaeta, “Octave-spanning frequency comb generation in a silicon nitride chip,” *Opt. Lett*. **36**, 3398-3400 (2011).

[17] J. Lim. S. W. Huang, A. K. Vinod, P. Mortazavian, M. Yu, D.-L. Kwong, A. A. Savchenkov, A. B. Matsko, L. Maleki, and C. W. Wong, “Stabilized chip-scale Kerr frequency comb via a high-Q reference photonic microresonator,” *Opt. Lett.* **41**, 3706 (2016).

[18] S.-W. Huang, A. K. Vinod, J. Yang, M. Yu, D.-L. Kwong, and C. W. Wong, “Quasi-phase-matched multispectral Kerr frequency comb,” *Opt. Lett*. **42**, 2110 (2017).

[19] S.-W. Huang, J. Yang, S. H. Yang, M. Yu, D.-L. Kwong, T. Zelevinsky, M. Jarrahi, and C. W. Wong, “Globally stable microresonator Turing pattern formation for coherent high-power THz radiation on-chip,” *Phys. Rev. X*. **7**, 041002 (2017).

[20] H. Zhou, Y. Geng, W. Cui, S.-W. Huang, Q. Zhou, K. Qiu, and C. W. Wong, “Soliton bursts and deterministic dissipative Kerr soliton generation in auxiliary-assisted microcavities,” *Light Sci. Appl*. **8**, 50 (2019).

[21] Y. Li, S.-W. Huang, B. Li, H. Liu, J. Yang, A. K. Vinod, K. Wang, M. Yu, D.-L. Kwong, H. T. Wang, K. K. Y. Wong, and C. W. Wong, “Real-time transition dynamics and stability of chip-scale dispersion-managed frequency microcombs,” *Light Sci. Appl*. **9**, 52 (2020).

[22] J. Yang, S. W. Huang, Z. Xie, M. Yu, D.-L. Kwong, and C. W. Wong, “Coherent satellites in multispectral regenerative frequency microcombs,” *Commun. Phys*. **3**, 27 (2020).

[23] A. K. Vinod, S.-W. Huang, J. Yang, M. Yu, D.-L. Kwong, and C. W. Wong, “Frequency microcomb stabilization via dual-microwave control,” *Commun. Phys*. **4**, 81 (2021).

[24] S.-W. Huang, J. Yang, M. Yu, B. H. Mcguyer, D.-L. Kwong, T. Zelevinsky, and C. W. Wong, “A broadband chip-scale optical frequency synthesizer at 2.7 10-16 relative uncertainty,” *Science Adv*. **2**, 4 (2016).

[25] M. H. P. Pfeiffer, C. Herkommer, J. Liu, H. Guo, M. Karpov, E. Lucas, M. Zerva, and T. J. Kippenberg, “Octave-spanning dissipative Kerr soliton frequency combs in Si3N4 microresonators,” *Optica* **4**, 684 (2017).

[26] X. Xue, Y. Xuan, Y. Liu, P. H. Wang, S. Chen, J. Wang, D.E. Leaird, M. Qi, and A. M. Weiner, “Mode-locked dark pulse Kerr combs in normal-dispersion microresonators,” *Nat. Photonics* **9**, 594–600 (2015).

[27] B. Yao, S.-W. Huang, Y. Liu, A. K. Vinod, C. Choi, M. Hoff, Y. Li, M. Yu, Z. Feng, D.-L. Kwong, Y. Huang, Y. Rao, X. Duan, and C. W. Wong, “Gate-tunable frequency combs in graphene–nitride microresonators,” *Nature* **558**, 410-414 (2018).

[28] J. M. Chavez Boggio, D. Bodenmüller, S. Ahmed, S. Wabnitz, D. Modotto, and T. Hansson, “Efficient Kerr soliton comb generation in micro-resonator with interferometric back-coupling,” *Nat. Comm*. **13**, 1292 (2022).

[29] S. Kar, M. Saha, S. K. Bag, R. K. Sinha, S. Sharma, S. Singhal, and S. K. Varshney, “Cold-resonance-mediated self-stabilization of Kerr frequency combs in a Si3N4 microring resonator,” *Phys. Rev. A* **106**, 013517 (2022).

[30] H. Jung, C. Xiong, K. Y. Fong, X. Zhang, and H. X. Tang, “Optical frequency comb generation from aluminum nitride microring resonator,” *Opt. Lett.* **38**, 2810 (2013).

[31] B. J. M. Hausmann, I. Bulu, V. Venkataraman, P. Deotare, and M. Lončar, “Diamond nonlinear photonics,” *Nat. Photonics* **8**, 369–374 (2014).

[32] M. Pu, L. Ottaviano, E. Semenova, and K. Yvind, “Efficient frequency comb generation in AlGaAs-on-insulator,” *Optica* **3**, 823 (2016).

[33] C. Y. Wang, T. Herr, P. Del’Haye, A. Schliesser, J. Hofer, R. Holzwarth, T.W. Hänsch, N. Picqué, and T. J. Kippenberg, “Mid-infrared optical frequency combs at 2.5 μm based on crystalline microresonators,” *Nat. Commun.* **4**, 1345 (2013).

[34] I. S. Grudinin, N. Yu, and L. Maleki, “Generation of optical frequency combs with a CaF2 resonator,” *Opt. Lett.* **34**, 878–880 (2009).

[35] 1. T. E. Drake, T. C. Briles, J. R. Stone, D. T. Spenser, D. R. Carlson, D. D. Hickstein, Q. Li, D. Westly, K. Srinivasan, S. A. Diddams, and S. B. Papp, “Terahertz-Rate Kerr-Microresonator Optical Clockwork,” *Phys. Rev. X* **9**, 031023 (2019).

[36] A. K. Vinod, S.-W. Huang, J. Yang, M. Yu, D.-L. Kwong, and C. W. Wong, "Frequency microcomb stabilization via dual-microwave control," *Comm. Phys.* **4**, 81 (2021).

[37] S. T. Cundiff, and J. Ye, “Colloquium: Femtosecond optical frequency combs,” *Rev. Mod. Phys*. **75**, 325–342 (2003).

[38] J. Yang, S.-W. Huang, Z. Xie, M. Yu, D.-L. Kwong, and C. W. Wong, "Coherent satellites in multispectral regenerative frequency microcombs," *Comm. Phys.* **3**, 27 (2020).

[39] T. M. Fortier, M. S. Kirchner, F. Quinlan, J. Taylor, J. C. Bergquist, T. Rosenband, N. Lemke, A. Ludlow, Y. Jiang, C. W. Oates, and S. A. Diddams, “Generation of ultrastable microwaves via optical frequency division,” *Nature Photon* **5**, 425–429 (2011).

[40] H. Guo, M. Karpov, E. Lucas, A. Kordts, M. H. P Pfeiffer, V. Brasch, G. Lihachev, V. E. Lobanov, M. L. Gorodetsky, and T. J. Kippenberg, “Universal dynamics and deterministic switching of dissipative Kerr solitons in optical microresonators,” *Nature Phys* **13**, 94–102 (2017)

[41] W. Drexler and J. Fujimoto “Optical Coherence Tomography: Technology and Applications” Berlin, Germany: Springer; 2008

[42] A. F. Fercher, W. Drexler, C. K. Hitzenberger, and T. Lasser, “Optical coherence tomography,” *Rep. Prog. Phys*. **66**, 239–303 (2003).

[43] J. F. Bille, “High resolution imaging in microscopy and ophthalmology: New frontiers in biomedical optics”, Cham: Springer International Publishing (2019).

[44] S. H. Kassani, M. Villiger, N. Uribe-Patarroyo, C. Jun, R. Khazaeinezhad, N. Lippok, and B. E. Bouma, “Extended bandwidth wavelength swept laser source for high resolution optical frequency domain imaging,” *Opt. Express* **25**, 8255–8266 (2017).

[45] B. J. Vakoc, R. M. Lanning, J. A. Tyrrell, T. P. Padera, L. A. Bartlett, T. Stylianopoulos, L. L. Munn, G. J. Tearney, D. Fukumura, R. K. Jain, and B. E. Bouma, “Three-dimensional microscopy of the tumor microenvironment in vivo using optical frequency domain imaging,” *Nat. Med*. **15**, 1219–1223 (2009).

[46] T. Bolmont, A. Bouwens, C. Pache, M. Dimitrov, C. Berclas, M. Villiger, B. M. Wegenast-Braun, T. Lasser, and P. C. Fraering, “Label-free imaging of cerebral β -amyloidosis with extended focus optical coherence microscopy,” *J. Neurosci*. **32**, 14548–14556 (2012).

[47] V. J. Srinivasan, H. Radhakrishnan, J. Y. Jiang, S. Barry, and A. E. Cable, “Optical coherence microscopy for deep tissue imaging of the cerebral cortex with intrinsic contrast,” *Opt. Express* **20**, 2220–2239 (2012).

[48] D. Huang, E. A. Swanson, C. P. Lin, J. S. Schuman, W. G. Stinson, W. Chang, M. R. Hee, T. Flotte, K. Gregory, C. A. Puliafito, and J. G. Fujimoto, “Optical Coherence Tomography,” *Science* **254**, 1178–1181 (1991)

[49] Z. Yaqoob, J. Wu, and C. Yang, “Spectral domain optical coherence tomography: a better OCT imaging strategy,” *BioTechniques* **39**, S6–S13 (2005)

[50] T. Bajraszewski, M. Wojtkowski, M. Szkulmowski, A. Szkulmowska, R. Huber, and A. Kowalczyk, “Improved spectral optical coherence tomography using optical frequency comb,” *Opt. Express, OE* **16,** 4163–4176 (2008)

[51] M. Siddiqui, A. S. Nam, S. Tozburun, N. Lippok, C. Blatter, and B. J. Vakoc, “High-speed optical coherence tomography by circular interferometric ranging,” *Nature Photon* **12,** 2 (2018)

[52] X. Ji, X. Yao, A. Klenner, Y. Gan, A. L. Gaeta, C. P. Hendon, and M. Lipson, “Chip-based frequency comb sources for optical coherence tomography,” *Opt. Express, OE* **27,** 19896–19905 (2019), doi

[53] P. J. Marchand, J. Riemensberger, J. C. Skehan, J.-J. Ho, M. H. P. Pfeiffer, J. Liu, C. Hauger, T. Lasser, and T. J. Kippenberg, “Soliton microcomb based spectral domain optical coherence tomography,” *Nat Commun* **12,** 427 (2021)

[54] X. Yao, “Ultrahigh resolution spectral domain optical coherence tomography and its functional extension for human myocardium and breast tissue imaging,” Columbia University (2018)

[55] X. Yao, Y. Gan, C. C. Marboe, and C. P. Hendon, “Myocardial imaging using ultrahigh-resolution spectral domain optical coherence tomography,” *JBO* **21,** 061006 (2016)

[56] G. Lihachev, J. Liu, W. Weng, L. Chang, J. Guo, J. He, R. N. Wang, M. H. Anderson, J. E. Bowers, and T. J. Kippenberg, “Platicon microcomb generation using laser self-injection locking,” *Nat. Comm* **13**, 1771 (2021)

[57] M. H. Anderson, G. Lihachev, W. Weng, J. Liu, and T. J. Kippenberg, “Zero-dispersion Kerr solitons in optical microresonators,” *Nat. Comm.* **13**, 4764 (2020)

[58] H. W. Shu, L. Chang, H. Lao, B. T. Shen, W. Q. Xie, X. G. Zhang, M. Jin, Y. S. Tao, R. X. Chen, Z. H. Tao, S. H. Yu, Q.-F. Yang, X. J. Wang, and J. E. Bowers, “Sub-milliwatt, widely-tunable coherent microcomb generation with feedback-free operation”, *Adv. Photon.* **5**, 036007 (2023).

[59] S.-W. Huang, H. Liu, J. Yang, M. Yu, D.-L. Kwong, and C. W. Wong, “Smooth and flat phase-locked Kerr frequency comb generation by higher order mode suppression”, *Sci. Rep.* **6**, 26255 (2016).

[60] D. J. Jones, Y. Chen, H. A. Haus, and E. P. Ippen, “Resonant sideband generation in stretched-pulse fiber lasers”, *Opt. Lett.* **23**, 1535-1537 (1998).

[61] Q.-F. Yang, Q.-X. Ji, L. Wu, B. Shen, H. Wang, C. Bao, Z. Yuan, and K. Vahala, “Dispersive-wave induced noise limits in miniature soliton microwave sources”, *Nat. Commun.* **12**, 1442 (2021).